SURROGATE MODELS FOR THE DESIGN AND CONTROL OF SOFT MECHANICAL SYSTEMS

BY

SREE SHANKAR SATHEESH BABU

DISSERTATION

Submitted in partial fulfillment of the requirements
for the degree of Doctor of Philosophy in Systems and Entrepreneurial Engineering
in the Graduate College of the
University of Illinois at Urbana-Champaign, 2019

Urbana, Illinois

Doctoral Committee:

Assistant Professor Girish Krishnan, Chair
Professor Thenkurussi Kesavadas
Associate Professor Ramavarapu S Sreenivas
Assistant Professor Aimy Wissa

ABSTRACT

Soft mechanical systems constitute stretchable skins, tissue-like appendages, fibers and fluids, and utilize material deformation to transmit forces or motion to perform a mechanical task. These systems may possess infinite degrees of freedom with finite modes of actuation and sensing, and this creates challenges in modeling, design and controls. This thesis explores the use of surrogate models to approximate the complex physics between the inputs and outputs of a soft mechanical system composed of a ubiquitous soft building block known as Fiber Reinforced Elastomeric Enclosures (FREEs). Towards this the thesis is divided into two parts, with the first part investigating reduced order models for design and the other part investigating reinforcement learning (RL) framework for controls.

The reduced order models for design is motivated by the need for repeated quick and accurate evaluation of the system performance. Two mechanics-based models are investigated: (a) A Pseudo Rigid Body model (PRB) with lumped spring and link elements, and (b) a Homogenized Strain Induced (HIS) model that can be implemented in a finite element framework. The parameters of the two models are fit either directly with experiments on FREE prototypes or with a high fidelity robust finite element model. These models capture fundamental insights on design by isolating a fundamental dyad building block of contracting FREEs that can be configured to either obtain large stroke (displacement) or large force. Furthermore, the thesis proposes a novel building block-based design framework where soft FREE actuators are systematically integrated in a compliant system to yield a given motion requirement. The design process is deemed useful in shape morphing adaptive structures such as airfoils, soft skins, and wearable devices for the upper extremities.

Soft robotic systems such as manipulators are challenging to control because of their flexibility, ability to undergo large spatial deformations that are dependent on the external load. The second part of this work focuses on the control of a unique soft continuum arm known as the BR^2 manipulator using reinforcement learning (RL). The BR2 manipulator has a unique parallel architecture with a combined bending mode and torsional modes, and its inherent asymmetric nature precludes well defined analytical models to capture its forward kinematics. Two RL-based frameworks are evaluated on the BR^2 manipulator and their efficacy in carrying out position control using simple state feedback is reported in this work. The results highlight external load invariance of the learnt control policies which is a significant factor for deformable continuum arms for applications involving pick and place operations. The manipulator is deemed useful in berry harvesting and other agricultural applications.

This thesis is dedicated to my father, who taught me that the best kind of knowledge to have is that which is learned for its own sake, my mother, who taught me that even the largest task can be accomplished if it is done one step at a time and my sister who supported me in the hardest of times.

ACKNOWLEDGEMENTS

I would like to express the deepest appreciation to my committee chair Dr Girish Krishnan, who has the attitude and the substance of a genius: he continually and convincingly conveyed a spirit of adventure regarding research. Without his guidance and persistent help this dissertation would not have been possible. I would like to thank my committee members, Dr Thenkurussi Kesavadas, Dr Ramavarapu S Sreenivas and Dr Aimy Wissa for their valuable insight, guidance and support in steering this work to a timely completion.

TABLE OF CONTENTS

CHAPTER 1: INTRODUCTION

Fiber-Reinforced Elastomeric Enclosures (FREEs) are hollow cylinders reinforced by a network of two families of fibers (α and β respectively) as shown in Figure 1(a) [1], [2]. When pressurized with fluids, FREEs enable different motion patterns such as bending, extension, rotation, and spiral motion depending on the relative fiber orientations. In this work, we limit our attention to a specific class of FREEs that have symmetric fiber angles (α = - β), and thus contract in length upon actuation as shown in Figure 1(b-c). Known as McKibben pneumatic muscles, they have been used as biomimetic actuators in robotics for over two decades.

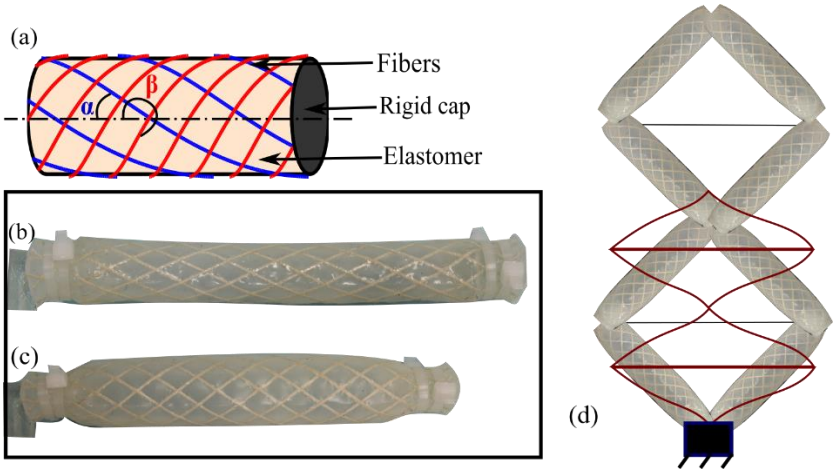

Figure 1: (a) Constituents of FREEs, and (b) undeformed (c) deformed configuration of contracting FREEs and (d) pennate arrangement of FREEs

The motivation of this work stems from the need to analyze systems of soft elements interconnected in complex architectures that leverages increased performance benefits realized by the topology of the network. For example, Figure 1(d) shows several FREEs arranged in a dyadic or pennate configuration like the fiber strands in a muscle. The net actuation stroke is more than five times the stroke of a single FREE, implying large possible amplifications or gear ratios that can result from planar or spatial topological connections. The resulting performance benefits are

due to the FREEs acting as both actuators that contract, and structural members that bend or flex to ensure overall system compatibility. While several models exist to capture the axial contracting actuation of FREEs [3], [4] few models take into account their bending behavior due to transverse loads or moments. Trivedi and Rahn [5], [6] treat the bending of extending FREEs as Cosserat rods [7] with linear elastic material properties, and decouple actuation forces from the bending mechanics. Walker et al. [8] introduced discrete or lumped approaches to model continuum arms. However, these models are accurate only when the systems of FREEs are co-axial as in continuum manipulators and cannot be directly extended to a system of FREEs in a planar or spatial network. Furthermore, these models do not take into account the changes in geometry (area of cross-section and elastic properties) that result due to internal pressurization of contracting FREEs.

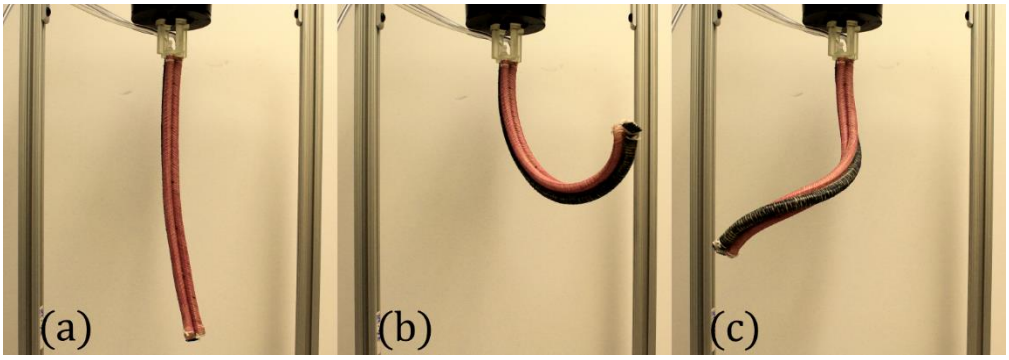

Figure 2: Deformation modes available to a BR^2 soft manipulator. (a) Home position at zero pressure, (b) Bending FREE pressurized and (c) Bending and rotating FREE pressurized

The second part of this work focuses on the control of a unique soft continuum arm known as the BR^2 manipulator [9], [10] using reinforcement learning. The BR^2 has a completely parallel architecture from an asymmetric combination of FREEs that bend and rotate simultaneously, the combination of which yields a spatial deformation pattern as shown in Figure 2. The advantage of this architecture is its ability to bend spatially to avoid obstacles and use its whole arm towards grasping long and slender objects by spirally deforming around them, while still maintaining a

parallel architecture. Control of soft continuum arms have been widely explored through both model based and model free methods [11]. Traditional control methods are founded on first-principles based on mathematical models and use of analytical equations to capture the exact behavior within bounding assumptions [12]–[14]. Mathematical models achieve great accuracy and stability if the assumptions made while deriving their governing equations remain valid. The realm of model free methods is dominated by machine learning techniques. Both supervised and reinforcement learning have been used to address control problems of varying levels of difficulty. Supervised learning has been used to fit artificial functions that maps inputs to outputs for estimating inverse kinematics and dynamics of robots in settings such as neuro-adaptive model-reference adaptive control. In the context of soft robots, frameworks such as feed forward neural nets, and more recently recurrent neural nets [11] have been used to characterize dynamic properties of different soft manipulators. While using neural networks makes the process of modeling simple, it is subject to issues like over-fitting and requires a good evaluation mechanism to guarantee stability of the control policy. This makes the process of training each robot different as the input-output mapping may vary for different prototypes. The same issue arises if the robots are subjected to external loads, which have been shown to impact the workspace of the BR^2 manipulator. Towards addressing the complexities addressed above this works presents the use of simplified surrogate models for the design, analysis and control of mechanisms derived from soft elements.

1.1 Problem Statements

Drawing inspiration from the need for suitable frameworks for the design, analysis and control of soft mechanical systems, the objectives of this work is stated as

1. ***The use of surrogate modeling techniques to accurately capture force-deformation characteristics of systems of Fiber Reinforced Elastomeric Enclosures (FREEs), and***
2. ***To adapt principles of reinforcement learning for the generalized position control of an asymmetric soft spatial continuum arm termed as the BR^2 manipulator.***

A surrogate model is a compact analytic model that approximates the multivariate input/output behavior of complex systems using a limited set of computationally expensive simulations. Three steps involved in creating a robust surrogate model are: (1) Selecting samples from experiments, (2) Constructing a suitable model with appropriate number of parameters to capture non-linearities effectively and (3) Optimizing and appraising the model for accuracy. This work explores the use of surrogate models to approximate the complex physics between the inputs and outputs of soft systems. To develop a suitable surrogate model for design and analysis of FREE-based systems the following steps are followed: (1) creation of a robust and experimentally validated high-fidelity finite element model which is then used to gather sample data points, (2) proposing surrogate formulations for capturing non-linear responses of FREEs. This work focuses on two such formulations, and (3) fitting and validation of the surrogate parameters. The surrogate formulations must be scalable to large networks of FREEs and adaptable in simulation-based optimization frameworks. We use artificial neural networks (NN) to as a suitable surrogate formulation to capture the complex kinetostatic behavior of the BR^2 manipulator. As before three steps are followed to obtain a robust surrogate model: (1) collection of sample data from analytical simulation or physical prototype, (2) tuning the weights of the NN to effectively map inputs and outputs of the BR^2 and (3) validation of NN for random inputs. The application of NN to capture transition kinetostatics during position control of the BR^2 is done using principles from reinforcement learning and not traditional supervised learning.

1.2 Related Work

Reduced Order Models: While several models exist to capture the axial contracting actuation of FREEs [15]–[19] few models take into account their bending behavior due to transverse loads or moments. Trivedi and Rahn [20], [21] treat the bending of extending FREEs as Cosserat rods [7] with linear elastic material properties, and decouple actuation forces from the bending mechanics. Walker et al. [22], [23] introduced discrete or lumped approaches to model continuum arms. However, these models are accurate only when the systems of FREEs are co-axial as in continuum manipulators [24], and cannot be directly extended to a system of FREEs in a planar or spatial network. Furthermore, these models do not take into account the changes in geometry (area of cross-section and elastic properties) that result due to internal pressurization of contracting FREEs. We exploit a reduced order model developed for simulating large deflections in planar compliant beams known as Pseudo-Rigid-Body (PRB) model [25]–[27]. The term reduced-order is applicable in the context that in place of solving partial or ordinary differential equations to obtain deformation characteristics, the presented approach utilizes a non-linear algebraic formulation to capture the same behavior. Hence, there is a reduction in order of complexity as compared to models derived using continuum mechanics. In a 3D setting, designing such systems can be a challenge as high-fidelity modeling and analysis tools, although accurate, can become computationally intensive. A preliminary study conducted by the authors to assess the increase in computation time as reported by a commercial FEA solver (ABAQUS) for soft fiber reinforced bending actuators [19] indicates a nonlinear trend that quickly becomes computationally intractable with more soft elements (Figure 3 (c)). One of the greatest challenges in analysis of soft robotic actuators is effective characterization of its nonlinear material properties that serve as inputs to mechanics-based models. For example, Cosserat rod models [28]–[30] model the large

deformation curvature space of slender continuum robots, but its accuracy is dependent on the material characterization and actuation models [31]. In the authors' earlier work we proposed a lumped pseudo-rigid body model to capture the bending behavior of contracting PAMs [32], and established that the stiffness of the PAM changes with its internal pressurization or actuation. Similar coupling between stiffness and actuation have been studied for applications as reported by [33]–[35]. From Figure 3 it can be observed that PRB models are more accurate and have lower computation time, however their analysis is restricted to planar mechanisms.

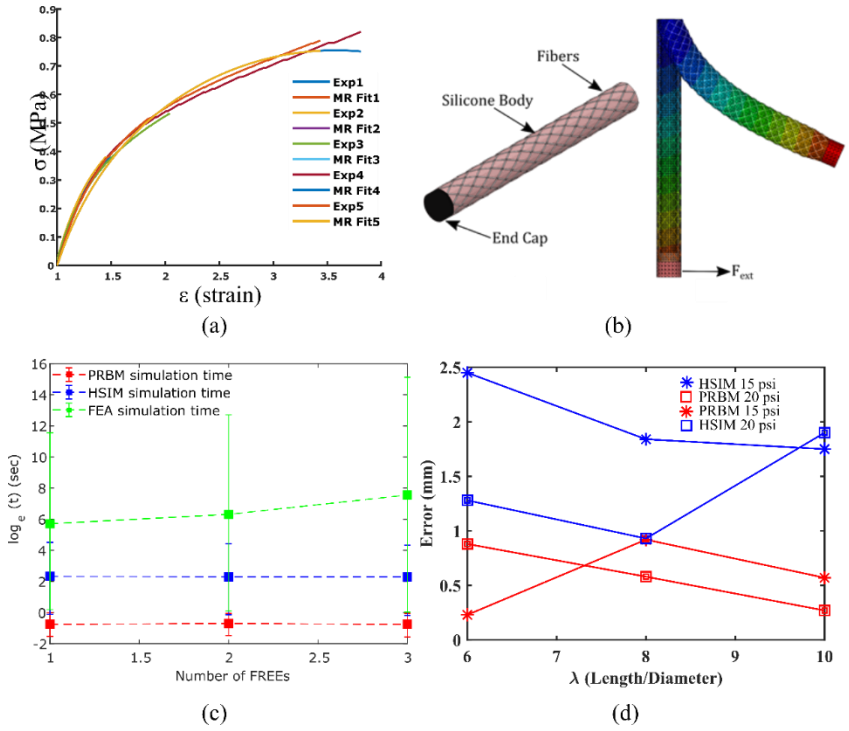

Figure 3: Preliminary study on increase in analysis time with number of FREEPAMs. (a) Material estimation and Mooney-Rivlin fit over repeated trials for latex used to manufacture FREEPAMs. (b)FEA rendering of FREEPAM subjected to transverse loading during parameter estimation of reduced-order models. (c) Variation in computation time as function of mechanism complexity and (d) Variation in fitting error for the two reduced-order models being investigated as a function of FREEPAM aspect ratio and actuation pressure.

In contrast, the Homogenized Strain Induced Model (HSIM) has higher computation time and lower accuracy but better suited for analyzing more complex spatial mechanisms in conjunction with commercially available CAD packages.

Architectured Systems: Networked systems are highly prevalent in nature and more commonly used in engineered structures and are made from deliberate arrangements of building blocks [36]. They are often associated with increased strength, reduced material usage and in certain cases yield non-intuitive deformation modes. Examples include, negative Poisson's ratio [37] and negative thermal expansion coefficients [38] that can be achieved using conventional materials tailored to a specific arrangement at the microscopic level. In the domain of structures that deform passively, nature presents several examples of actuators that serve as simple building blocks bundled together in a networked architecture to perform varying functions. A prime example in this regard are skeletal muscles of animals of which there are two types: “Fusiform” muscles, which generate greater contraction but lower forces, and are characterized by linearly arranged fibers and “Pennate” muscles that generate greater forces at lower strokes, and possess fibers that approach their central tendon obliquely [39][40]. By leveraging the geometric arrangement of these myofibers, muscle performance can be effectively tuned to either provide large forces or large stroke. In the engineering realm and actively actuated networks, Nawroj and Dollar [41], [42] used planar meshes of conventional linear motors and flexible connectors to morph surfaces into any desired shape. Similar concepts have also been demonstrated in the MEMS scale with electrostatic actuators [43]. Earlier research on shape morphing active compliant mechanisms with embedded actuation [44][45], adaptive grippers [46][47], and 3D tensegrity mechanisms capable of gait generation [48][49] also exhibit an architecture of active elements. Figure 4 details two systems that have been analyzed and designed using the models described in this thesis. The soft

components are approximated using reduced-order models and incorporated into existing analysis frameworks to generate design that are tailored to meet specific requirements. The use of such reduced-order models remains effective in spatial (sleeve) and planar (shape morphing mechanism) settings.

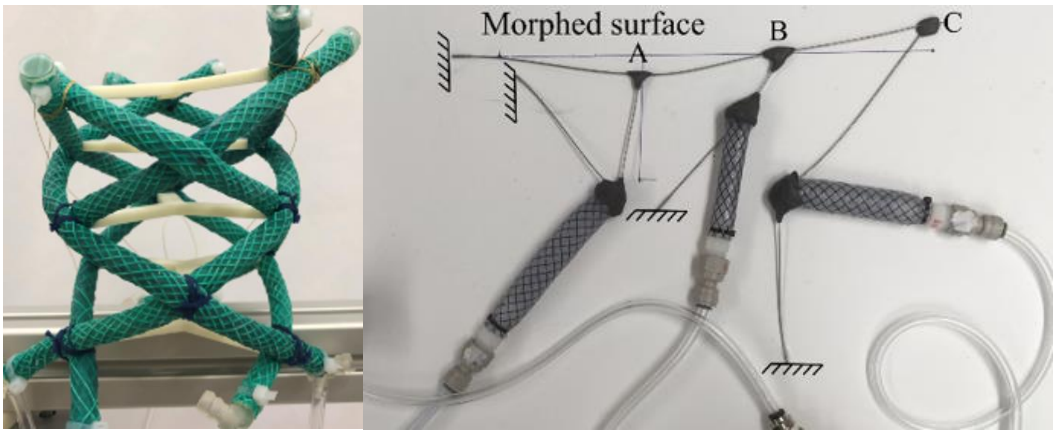

Figure 4: Design and analysis of soft mechanical systems. (a) Soft sleeve with displacement amplification properties and (b) a shape morphing mechanism with embedded actuation.

Learning-Based Control: There are several challenges in design of soft continuum arms that manifest as trade-offs in their performance attributes. For example, in continuum arms, achieving large workspace and dexterity may require serial combination of several building blocks or actuators that effectively reduces compactness, energy efficiency, and leads to bulky structures that are difficult to control. These were evident in OctArm [20], [24], one of the earliest soft and continuum manipulators which consisted of several serial modules of spatially bending segments. While multiple serial modules were required to obtain dexterity, large workspace and whole arm manipulations, this leads to excessive bulky designs whose achievable static workspace was attenuated due to gravity. Most continuum manipulators are slated to have a better dynamic workspace, but this may be unsuitable for applications that involve manipulation and may reduce safety during interaction. Some novel designs propose using stiffness modulating building blocks

that utilize granular jamming to improve the load bearing ability of the manipulator in the deformed configuration [50], [51]. Controlling SCAs is challenging because of their infinite degrees of freedom and the availability of limited sensing avenues. Most existing control strategies can be broadly divided into three categories: (i) classical model based methods, (ii) model based learning methods, and (iii) model free learning methods [52]. Classical model based controls traditionally build on accurate analytical expressions for forward kinematics and rapid evaluations of inverse kinematics [53]. In the context of SCAs, these approaches are bounded by certain assumptions. Primary among them is the constant curvature assumption that enables such a control schemes to be adapted for SCAs albeit with greater inaccuracies when accounting for factor that violate the assumption (Ex: external loads that distort the deformation geometry). Model based learning methods circumvent analytical formulations for forward kinematics by fitting an experimental data-driven Artificial Neural Network (ANN). However, obtaining the inverse kinematics directly from a model offers challenges including discontinuity of the work space [54], stability of points lying outside the reachable workspace and load dependencies of learned policies. Thuruthel et al. [55] adopted a differential inverse kinematics approach using spatially localized exploration that addressed some of these limitations. In a more recent effort, Thuruthel et al. [11] presented a framework that learns the optimal policies in a dynamic closed loop setting operating on a learnt ANN forward model. While these methods are simple, effective, and easier to train with very few data points their performance on more complex SCAs with elements of discontinuity in workspace and complex interplay between soft members (due to contact) remains to be explored. Model free learning approaches requires large data sets for training but exhibit better optimal asymptotic performance [56]. Reinforcement learning (RL), and specifically the model-free Q-learning approach has been explored previously [57], [58] for static position control and

the studies were limited to planar manipulation tasks with discretized actions available to the system. Prior work [59] has also been done on adopted model-free Q learning method towards modeling multiple objectives using a multi-agent framework. A continuous alternative for model-free reinforcement learning based controls has been proposed using deep deterministic policy gradients (DDPG) [60], which can potentially scale well for systems with larger state-action spaces. To the authors' best knowledge this method has not been implemented in soft continuum manipulators due the large data sets required to train the model. The requisite sample sizes are often large enough to render this approach impractical to be directly used on a prototype. While training on a simulated model is possible, effectively transferring the model to the prototype under realistic, load bearing conditions with disturbance has not been investigated. Figure 5 showcases the learning-based framework explored in this work. The soft robot is trained in a rough simulation and the learned control policy is then deployed in a prototype in conjunction with state feedback from a motion capture system and the efficacy of the approach is validated in term of path tracking accuracy in the presence of external tip loading.

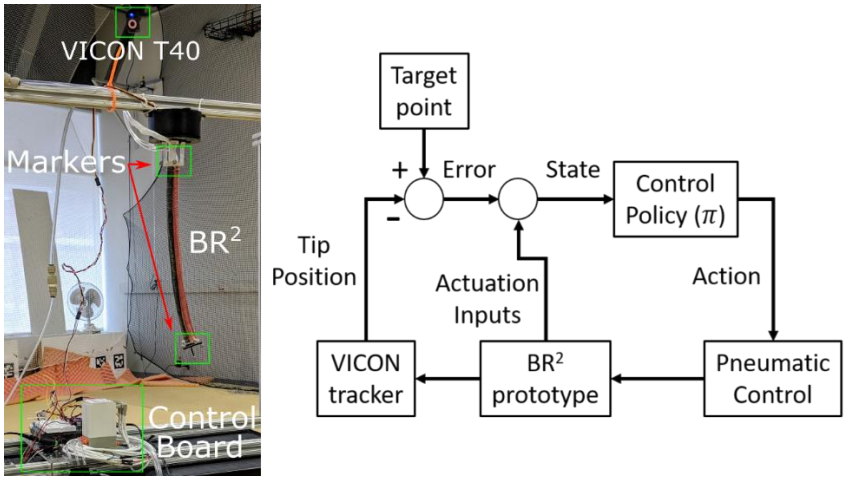

Figure 5: Learning-based framework for training in simulation and deploying in prototype

This thesis presents the incorporation of surrogate model into the analysis of soft mechanical systems to enable design ideation, analysis and control. In this regard the presented work is categorized as follows. Chapter 2 introduces the concept of surrogate/ reduced-order models and presents results form an in-depth analysis of two models and their applicability in the analysis of soft mechanical systems. Chapter 3 details the utility of the surrogate models for designing and analyzing systems of soft actuators arranged in architectures. This chapter also delves into the advantages of using architectures to leverage superior performance characteristics link stroke and force amplification. Chapter 4 explore the use of learning-based control in the context of soft robots and their robustness to environmental uncertainty. The learned control policy is validated in simulation and a prototype. Lastly, Chapter 5 enumerates the contributions made in this work and highlights a future path along which certain aspects of the work maybe extended.

CHAPTER 2: SURROGATE MODELS FOR SOFT ACTUATORS

The innate complexity of traditional continuum-based models makes the analysis of complex soft mechanical system with several soft elements intractable. Towards addressing this topic, this chapter presents an in-depth investigation into two reduced order models that have low fidelity, reduced computation time and easily scalable for systems of interconnected FREEs. This first model termed as the Pseudo-Rigid Body (PRB) Model was developed for analyzing compliant mechanisms and currently extended to analysis of FREEs and the second model termed as the Homogenized Strain Induced Model (HSIM) is a newly introduced model incorporating principles of nonlinear spatial beam deformation in conjunction with temperature gradients to accurately capture stroke-force properties of FREEs.

2.1 The Pseudo-Rigid Body (PRB) Model

The PRB model of length L selected in this investigation comprises of two linear and torsional springs connected to a rigid segment (Figure 6). The PRB model is described by four parameters: torsional spring stiffness (K_{th}), (2) linear spring stiffness (K_{ex}), (3) length of rigid segment as a fraction of undeformed FREE length (g) and (4) actuation force acting on the linear springs (fa). The torsional springs behave like revolute joints and capture stiffness associated with the ending behavior of the FREEs. The linear springs are assumed to have an undeformed length of lo and models the stiffness associated with axial length changes. The actuation of FREEs result from the internal pressurization leading to contraction in length. This is modeled as an actuation force acting on the linear spring stiffness. A similar model was presented in [32] with differences primarily in the placement of the linear and torsional springs. Experimentally this model is proved to be more accurate in capturing the curvilinear deformation profiles of the FREE.

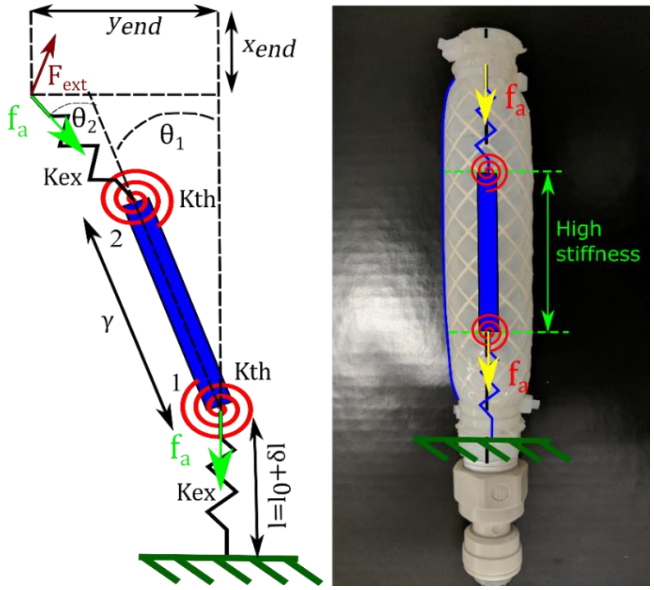

Figure 6: Serial link PRB Model with two torsional springs (revolute joints) and linear springs (prismatic joints)

We are interested in the tip position of the FREE as a function of internal actuation loads and transverse bending loads. The tip position is determined using forward kinematic equations (Eq. (1)) of the PRB model, and is a function of the joint angles, linear spring displacement and actuation force.

$$x_{tip} = (l_o + \delta l) + \gamma L cos(\theta_1) + (l_o + \delta l) cos(\theta_1 + \theta_2)$$
$$y_{tip} = \gamma L sin(\theta_1) + (l_o + \delta l) sin(\theta_1 + \theta_2) \quad (1)$$
$$\theta = \theta_1 + \theta_2$$

θ_1 and θ_2 are the angular deflections at the joints and dl is the linear spring deflections. The joint deflections are calculated using energy equivalence (Eq. (2)).

$$\tau = J^T F \quad (2)$$

where the joint torques, $t = (K_{th}\theta_1; K_{th}\theta_2; 2K_{ex}\delta l + 2fa)$ is related to the tip loads, $F_{tip} = (F_x, F_y, M_z)$ by the Jacobian of the PRB model, J. The Jacobian can be obtained by differentiating the terms of Eq. (1) [61]. To fit this PRB model for the FREE, we need to understand its axial and transverse

bending behavior. These can be obtained either experimentally or using Finite Element Analysis (FEA) [19]. While obtaining experimental data for different FREE sizes and shapes is tedious, we rely on fitting the PRB model on the FEA data. Towards this, we establish the accuracy of the FEA results by comparing it with experiments conducted on select FREEs. Details of the experimental testing method are explained in APPENDIX.

2.1.1 Fitting the PRB Model

In this section, we detail the steps used to validate the PRB models by comparing them with FE simulations. The PRB model parameters will be fit such that the difference between the tip deflection of the FREE evaluated from modeling and FE simulation is minimized. In our implementation, we use a multi-start gradient-based interior point search optimization routine (implemented in MATLAB R2016a) to optimally fit the PRB model parameters. An L2-norm based error function is minimized subjected to constraints that ensure the physical realizability of the PRB model. The fitting algorithm is run for a total of 27 times for every applied pressure, fiber angle and slenderness ratio.

$$\begin{aligned} &min\ \ f(\gamma, K_{th}, K_{ex}) = Err \\ &st.\ \ 0.1 \leq \gamma \leq 0.85 \\ &0 \leq K_{th} \leq 10 \\ &0 \leq K_{ex} \leq 10 \end{aligned} \tag{3}$$

Where

$$Err = \sqrt{\frac{\sum_{i=0}^{N} (x_{tip_i} - x_{tip_i}^{sim})^2 + (y_{tip_i} - y_{tip_i}^{sim})^2}{N}} \tag{4}$$

x_{tip_i} and y_{tip_i} are the x and y coordinates of the tip position for i^{th} load and N is the number of loads applied. The goodness of fit as a measure of the error function is tabulated in Table 1. When loaded the FREEs experience a maximum deflection in the range of $0 - 45\ \ mm$ along the x-axis

and $0 - 95\ mm$ along the y-axis. The residuals indicate that the PRB models perform well in capturing the axial and bending behaviors of FREEs over varying FREE parameters.

Table 1: PRB Model Fit Residuals (mm)

$\boldsymbol{\lambda}$	$\boldsymbol{P_a}$ $\boldsymbol{(psi)}$	$\boldsymbol{\alpha = 25^o}$	$\boldsymbol{\alpha = 30^o}$	$\boldsymbol{\alpha = 40^o}$
6	20	0.33	0.88	0.39
	17.5	0.30	0.87	0.73
	15.0	0.27	0.23	0.38
8.5	20	1.05	0.58	1.38
	17.5	0.25	0.74	1.46
	15.0	0.43	1.12	1.57
10	20	0.95	0.27	1.56
	17.5	0.66	0.49	0.97
	15.0	0.21	0.57	1.87

2.1.2 Effect of Elastic Properties on Model Parameters

The purpose of using the PRB model approach is to capture the deformation behavior (both axial and transverse) of FREEs using a lower order simpler model within acceptable error bounds. Since a FREE is an inflatable, its elastic properties are a function of the (i) actuation pressure, (ii) fiber angle α, and (iii) length to diameter ratio λ.

1. Dependence on actuation pressure: The spring constants K_{ex} and K_{th} is in general expected to increase with actuation pressure P_a. Figure 7 captures the increase in the stiffness values as a function of pressure in the range of testing pressures $(15 - 20\ psi)$. Furthermore, the kinematic parameter γ decides the fraction of the FREE length that deforms as a rigid

body. With actuation, the center of compliance of FREEs are pushed towards the ends due to the necking of the cross sections. The necking effect results due to constraining the ends from radial expansion resulting in a curvilinear deformation profile [3], [62]. The dependence of γ on actuation pressure is plotted in Figure 7, and is shown to be relatively invariant with applied pressure.

2. Dependence on fiber angle: The variation of the axial stiffness Kex as a function of the fiber angle is well documented in previous research [63]. In general, smaller fiber angles have larger axial and bending stiffness because of the resistance it poses against increase or decrease in FREE length due to contraction. This increase in stiffness is observed in Figure 7, but is more amplified in the axial stiffness Kex. Furthermore, the kinematic parameter γ depends on the increase in radius of the FREE. It is well known that FREEs with smaller fiber angles lead to a larger radial bulge upon pressurization as shown in Figure 8, thus leading to an increase in γ. Figure 7 clearly demonstrates the increase of γ as fiber angle decrease. A noticeable anomaly is observed for slenderness ratio λ=6 where $\alpha = 30^{\circ}$ has a lower value of γ than $\alpha = 40^{\circ}$. This could be attributed to dominant shearing effects present during bending that is common for short thick beams.
3. Dependence on length to diameter ratio: FREEs considered in this paper are slender cylinders that behave like elastic beams upon pressurization. Like beams, FREEs undergo bending under the action of transverse loads or bending moments. The bending stiffness of beams under the Euler-Bernoulli assumption decreases nonlinearly with increase in λ. We expect similar dependence of FREE stiffness on slenderness ratio. In Figure 7, it is seen that the values of the stiffness is smaller for larger slenderness ratio, keeping fiber angle is important to note that preliminary studies indicate that unlike K_{th} and K_{ex} the

effect of γ (within a certain range) on overall accuracy is minimal. and pressure the same. The kinematic parameter γ remains relatively constant with changing λ with the exception being very short beams with dominant shearing effects. It is important to note that preliminary studies indicate that unlike K_{th} and K_{ex} the effect of γ (within a certain range) son overall accuracy is minimal.

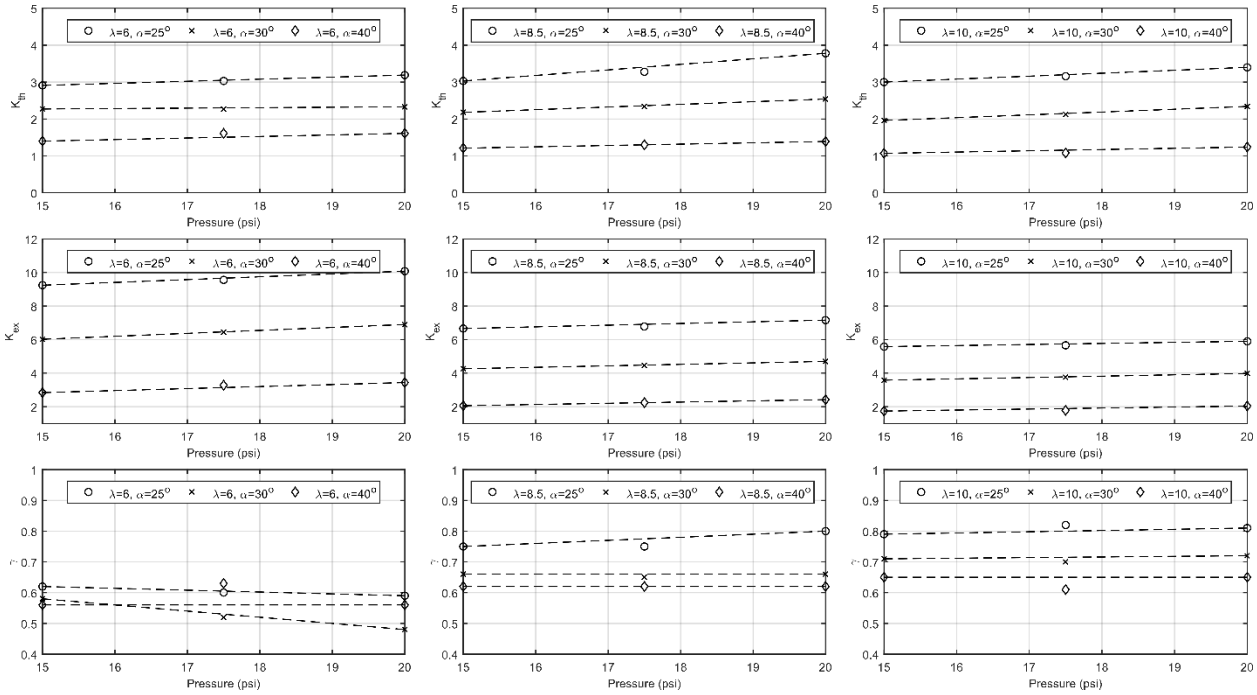

Figure 7: Variation in K_{th}, K_{ex} and γ with FREE parameters. Dotted lines represent linear trends.

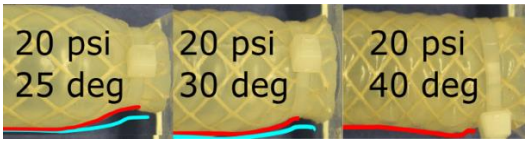

Figure 8: Radial bulge for FREEs with different fiber angles demonstrating the necking effect. Blue: Unpressurized and Red: Pressurized FREE profile

2.1.3 Parametric Model Fitting

Linear and quadratic regression models are proposed to capture the dependencies of the PRB parameters on actuation pressure, fiber angle and slenderness ratio as shown below in Eq. (5). Here, we assume that the number of fibers, external diameter, and wall thickness of the FREEs are assumed to be constant.

$$\begin{aligned} \gamma &= a_0 + a_1\lambda + a_2\alpha + a_3P_a + a_4\lambda^2 + a_5\alpha^2 + a_6P_a^2 \\ K_{th} &= b_0 + b_1\lambda + b_2\alpha + b_3P_a + b_4\lambda^2 + b_5\alpha^2 + b_6P_a^2 \\ K_{ex} &= c_0 + c_1\lambda + c_2\alpha + c_3P_a + c_4\lambda^2 + c_5\alpha^2 + c_6P_a^2 \end{aligned} \quad (5)$$

The linear model will use the first three coefficients while the nonlinear model will use all six coefficients. The best fit model is selected for the PRB model parameters based on the Akaike's Information Criterion (AIC). AIC provides a measure of model quality with the most accurate model having the smallest AIC value. The AIC values for first and second order models for the three parameters are tabulated in Table 2.

The AIC value for K_{th} is smaller for a linear model indicating a better fit that accurately captures the parametric behavior. However, the AIC values for γ and K_{ex} was observed to be smaller for a quadratic model indicating a more non-linear trend that requires second order terms to capture the parametric behavior.The parameters obtained from Eq. (3) are used to fit the nonlinear models defined in Eq. (5). The coefficient obtained from this fit are tabulated in Table 3. The goodness of fit can be determined by plotting the standardized residual plot of the data. As a rule of thumb, a good model present a symmetric distribution of standardized residuals centered on zero and is bounded to within ± 2 as seen in Figure 9.

Table 2: AIC-based model selection

AIC	**Model Order=1**	**Model Order=2**
γ	-88.24	-93.43
K_{th}	-4.16	-1.33
K_{ex}	17.81	9.22

Table 3: Parametric Model Coefficients

	$\boldsymbol{i=0}$	$\boldsymbol{i=1}$	$\boldsymbol{i=2}$	$\boldsymbol{i=3}$	$\boldsymbol{i=4}$	$\boldsymbol{i=5}$	$\boldsymbol{i=6}$
$\boldsymbol{\gamma\ (a_i)}$	1.5937	0.10667	-0.075852	-0.022	-0.0044444	0.0010519	0.00062222
$\boldsymbol{K_{th}\ (b_i)}$	5.4016	-0.072562	-0.12284	0.079778	–	–	–
$\boldsymbol{K_{ex}\ (c_i)}$	20.854	-0.82746	-0.70704	-0.061333	0.031074	0.0083259	0.0032

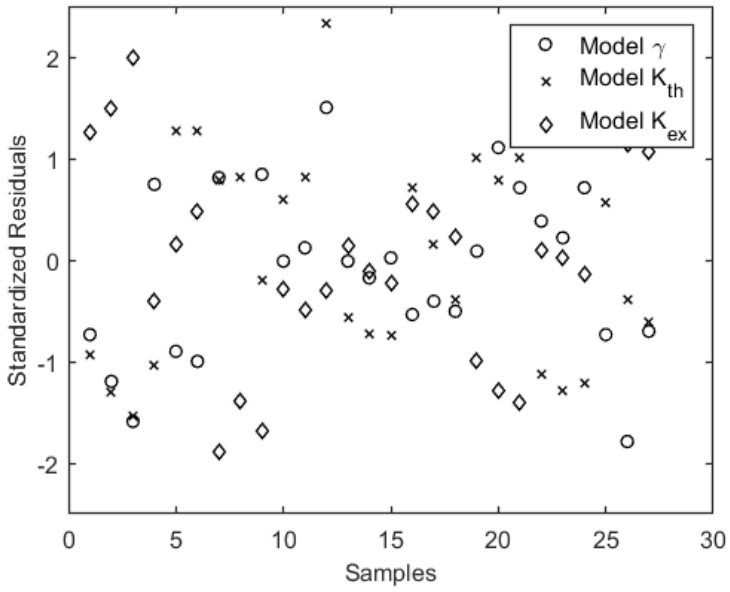

Figure 9: Standardized residuals for model fits

To demonstrate the efficacy of the model we need to assess its capability to generalize to FREEs defined within or outside the manifold from which the data was collected. We consider two configurations and mean tip position errors between the PRB model and FEM simulations for this study. The results are tabulated in Table 4.

Table 4: Generalization error

Time	**PRB Model Parameters**	**Tip Position Error** $(\boldsymbol{mm})$
$\lambda = 8.5, \alpha = 35^o, P = 15$ psi	$\gamma = 0.65$, $K_{th} = 1.68$, $K_{ex} = 2.64$	1.46
$\lambda = 8.5$, $\alpha = 45^o$, $P = 22.5$ psi	$\gamma = 0.61$, $K_{th} = 1.05$, $K_{ex} = 2.70$	3.40

It can be observed that the model error for an interpolated FREE is less than that of an extrapolated FREE. This indicates that by collecting data points uniformly or using techniques like Latin hypercube sampling (LHS) one can approximate the deformation characteristics of FREEs within that manifold with great degree of accuracy thereby circumventing the need for expensive simulations. This can become useful while creating conceptual designs having soft elements like FREEs.

2.2 The Homogenized Strain Induced Model (HSIM)

As explained before, Fiber Reinforced Elastomeric Enclosure Pneumatic Artificial Muscles or FREEPAMs are soft pneumatic actuators consisting of an inner bladder made from a hyper-elastic material and an outer layer of inextensible fibers constraining radial deformation. Both ends of FREEPAMs are capped to allow internal pressurization, which can cause contraction, elongation, bending, rotating or twisting depending on the angles of the inextensible fibers [62], [64], [65]. In this investigation, we are concerned with characterizing a contracting FREEPAM actuator, also referred to as the FREEPAM. When pressurized, the FREEPAM contracts, and simultaneously

undergoes radial expansion. This radial bulge tapers towards the ends as the FREEPAMs ends are fixed.

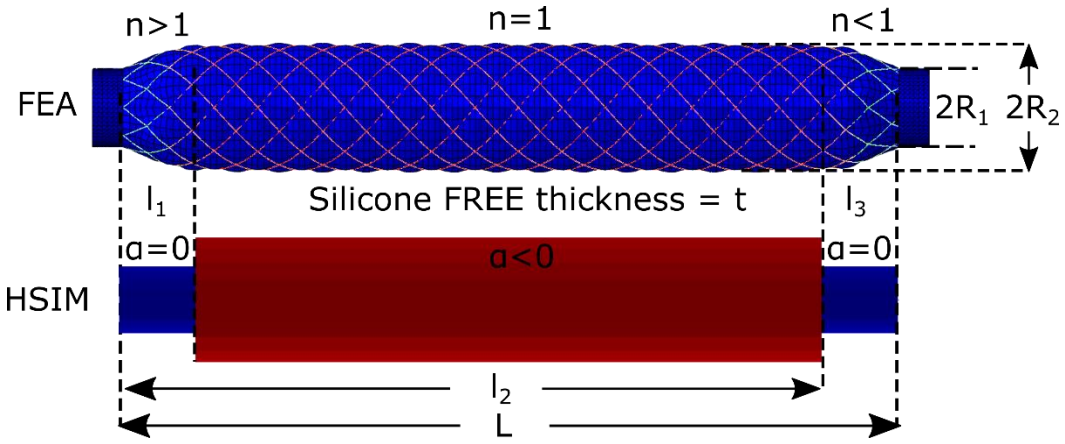

Figure 10: HSIM model morphology. (a) FEA rendering of deformed FREEPAM constrained at both ends. Pressurized FREEPAMs have two sections. The conical tip sections with non-zero taper and a middle cylindrical section with zero taper. (b) Configuration of HSIM analog to actuated FREEPAMs with a homogenized Young's modulus (E) and geometrical parameters R_1, R_2, t and contraction coefficient α.

To capture this deformed shape, the FREEPAM is modeled as a three-section Euler Bernoulli beam as shown in Figure 10, which include Section 1: Conical with a positive taper (l_1), Section 2: Cylindrical with no taper (l_2-l_1) and Section 3: Conical with negative taper(L-l_2). From Elastica theory, the bending of beams subjected to a concentrated tip load can be expressed as follows:

$$\frac{y''}{[1+(y')^2]^{\frac{3}{2}}} = -\frac{M_x}{E_o I_o f(x) g(x)} \qquad (6)$$

where M_x is the moment induced at intermediate sections, E_o, I_o are the Young's modulus and area moment of inertia at the tip and g(x), f(x) are the variations of E, I along the length of the beam. For a FREEPAM having constant Young's Modulus E, g(x)=1 and f(x) is derived as follows. For tapered sections, the variation in FREEPAM diameter is expressed as

$$d(l) = d_o[1 + \zeta l_o],\ \zeta = \begin{cases} \frac{n-1}{l_1}, 0 \le x < l_1 \\ \frac{n-1}{l_0}, l_1 \le x < l_2 \\ \frac{1-n}{l_3}, l_2 \le x < L \end{cases} \quad (7)$$

$$l_o = \int_0^x \sqrt{(1 + y'(x)^2)}dx \quad (8)$$

where l_o is the arc length of the section at a horizontal distance, x, from the tip, L is the total length of the beam, d_o is the tip diameter and n is the taper. Consequently, area moment of the FREEPAM approximation as a function of beam length can be defined by:

$$I(l) = I_0 f(x) = I_0[1 + \zeta l_0]^4 \quad (9)$$

Substituting Equation 9 in Equation 6, we obtain an exact nonlinear differentiable equation. The solution to Equation 8 becomes complex and requires good initial estimates of parameters to solve using iterative techniques. By approximating the tapered conical sections with cylindrical sections, Eq. (9) simplifies to Eq. (10).

$$f(x) = \begin{cases} d_{eff}, 0 \le x < l_1 \\ nd_{eff}, l_1 \le x < l_2 \\ d_{eff}, l_2 \le x < L \end{cases} \quad (10)$$

Thus, the nonlinear differential equation from Eq. (6) is simplified using a step variation in its cross section and can be solved iteratively using a nonlinear solver. The quality of solutions using this approximation depends on the quality of the estimates of the effective diameters of the three sections.

2.2.1 Model Parameters

The "Homogenized Strain Induced Model" (HSIM) has the following features:

- HSIM is used to approximate the kinetostatic stroke-force deformation characteristics of contracting FREEPAMs within some reasonable aspect ratio (length/diameter) bounds.
- HSIM is a data driven model, whose parameters are characterized from high fidelity finite element analysis models sampled at specified operating points.
- HSIM presents a homogenized version of a FREEPAM in terms of material properties and geometric characteristics.
- HSIM emulates internal strain generated during actuation using thermal equivalents.

Drawing parallels from actual deformed FREEPAM morphology, the HSIM has three sections, each capturing deformation effects unique to a region along the length of the FREEPAM. HSIM is characterized by the following tunable parameters:

- Geometry (t, R_1, R_2): Each section is assumed to be an annulus with a constant thickness t which is set to the thickness of the elastomer body of the FREEPAM. R_1, R_2 are the external radii of the two sections (first and third sections are assumed the same). R_1 represents an effective radius for capturing the effects of the conical end sections and R_2 is the effective radius of the cylindrical section described in section 2.1. Following the convention used in [66] and other related work, in our implementation the conical sections are assumed to have a length equal to the un-deformed diameter of the FREEPAM. A more involved surrogate model could have the section lengths included as tunable parameters.
- Effective Young's Modulus (E): The homogenized surrogate model is assumed to be made of a surrogate material having Young's Modulus, E. The surrogate material effectively captures the combined material effects of the hyper-elastic elastomer and inextensible fibers embedded within the elastomer. Different Young's Modulus values could be used for the conical and cylindrical sections to more accurately model nonlinear effects

associated with conical ends where localized shearing occurs during FREEPAM deformation.

- Thermal Contraction Coefficient, α: The surrogate material is assumed to have a tunable thermal contraction coefficient, α, that serves to induce strain that mimics the contraction of pressurized FREEPAMs. The conical sections have $\alpha = 0$ and the cylindrical section has $\alpha < 0$. When exposed to a temperature gradient (which is equal in magnitude to the applied internal pressure) the surrogate material contracts and generates a reaction force akin to blocked forces generated by FREEPAMs. Furthermore, having a single tunable parameter α simplifies the application of strain during global deformation analysis of networks of FREEPAMs and compliant constraints.

2.2.2 Data Collection

As described in Section 2.1, a high fidelity FEA (ABAQUS) simulation is used as the baseline for data collection. However, this could be substituted with experimental data from prototypes as an alternate. Each FREEPAM is initially pressurized and subjected to axial and bending tests by applying relevant tip loads and recording corresponding tip deflections. A python script in ABAQUS is used to extract and store relevant data. Collection of data is automated and can be performed for multiple actuation pressures within the same simulation. Data is collected for an actuation pressure ranging from 0.0689 MPa to 0.1724 Mpa (10-25 psi) in intervals of 0.0244 Mpa (5.0 psi). The lower limit of the interval corresponds to the minimum pressure at which this FREEPAM stops kinking when subjected to tip loads and the upper limit corresponds to the maximum actuation pressure at which the FREEPAM stops producing axial stroke. The temperature gradient analog (ΔT) for the operating range is thus set to 10-25 deg.

2.2.3 Optimization Framework

Within a network, interconnected FREEPAMs are subjected to two forms of loading: (1) Internal pressurization that leads to radial expansion, axial contraction and generation of force at the tip and (2) External tip loads that induced axial and transverse deflections. The tunable parameters of the HSIM work in tandem to capture the deformation modes associated with these two forms of loads. We adopt an optimization-based framework to obtain the best estimates of the HSIM parameters. The optimization framework (Figure 11) is detailed as follows:

- Optimization 1: The stroke generated by FREEPAMs are captured by α in the HSIM. Consequently, for a given input actuation pressure, α can be determined using a line search optimization. From elastica theory linear thermal expansion/contraction is defined as $\Delta l = \alpha \Delta T (l_2 - l_1)$, where Δl is the stroke generated and ΔT is the temperature gradient applied to a HSIM of length L. The temperature gradient is equal to the actuation pressure. A obtained from the above expression serves as a good initial guess for line search.
- Optimization 2: Axial and bending stiffness of FREEPAMs are a function of geometry and effective E of the material. Data from the axial and bending tests are used to optimize R_1, R_2 and E of the HSIM and a RMSE objective function (Eq. (11)) is adopted.

$$Err = \sqrt{\frac{\sum_{i=1}^{N}(x_{tip_i} - x_{tip_i}^{FEA})^2 + (y_{tip_i} - y_{tip_i}^{FEA})^2 + (\theta_{tip_i} - \theta_{tip_i}^{FEA})^2}{N}} \quad (11)$$

Where $x_{tip_i}, y_{tip_i}, \theta_{tip_i}$ are the x, y coordinates and slope of the tip for i^{th} tip load and N is the number of data points. A Nelder-Mead simplex method is used to obtain the local optimum. The base geometry of the FREEPAM is used to initialize R_1, R_2 for optimization while E is initialized as 1 Mpa obtained from preliminary studies. To reduce sensitivity to initial guess, each of the three

components of the objective function are scaled suitably. The optimization framework outputs the HSIM parameters as a function of temperature gradient (or pressure).

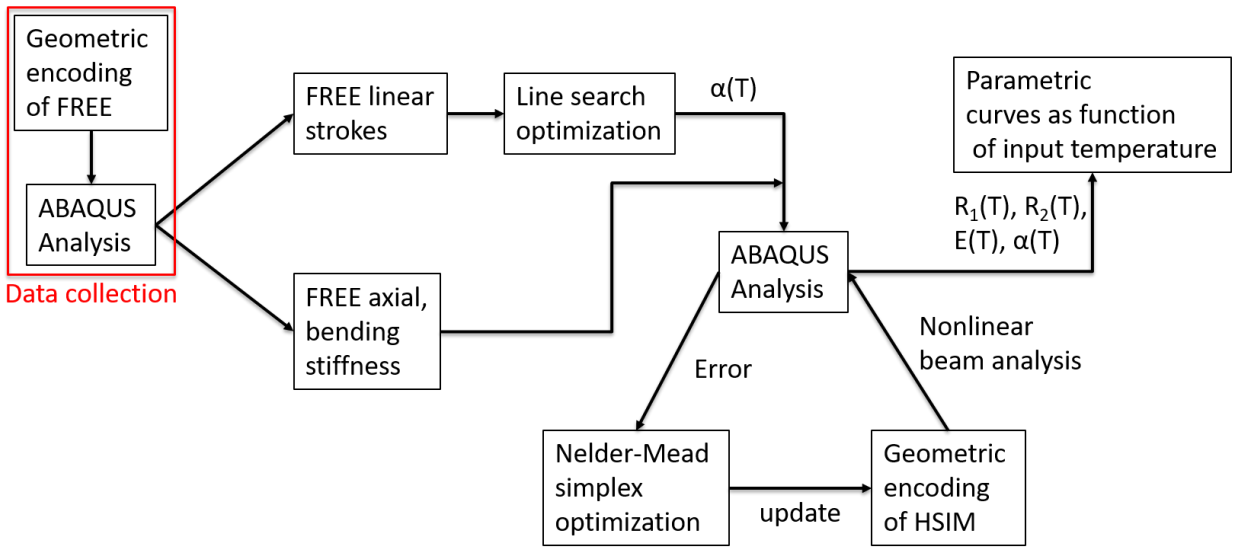

Figure 11: Estimation of HSIM parameters using an optimization framework. Estimated parameters correspond to local minima of optimization objective function. Consequently, there exists a one-to-many mapping between a FREEPAM and its HSIM.

2.2.4 Parametric Variation and Error Analysis

In this section we detail the efficacy of the HSIM in capturing the deformation characteristics of FREEPAMs. The results from the analysis is shown in Figure 12. Figure 12(a) describes the variation in the HSIM parameters with ΔT. The stiffness and stroke generated by FREEs increase with increase actuation pressure. Consequently, we observe an increase in E. α is observed to decrease as the generated axial stroke saturates with increase in ΔT. Lastly, the increase in R_1, R_2 is in accordance with the radial bulging of FREEPAMs at higher pressures. Figure 12 (b-d) details the error obtained from the HSIM for axial, bending deflections and tip slope. The HSIM reports errors of 0.8±0.18 mm for a maximum average axial stroke of 17.9 mm (4.4 %), 1.8±0.65 mm for a maximum average bending deflection of 73.6 mm (2.4 %) and 1.9±0.6 deg for a maximum

average slope of 55.3 deg (3.3 %) for a FREEPAM of aspect ratio 10. Figure 12 (b-d) also details the errors reported by FREEPAMs of different aspect ratios (6-14) using HSIM parameters tuned for a FREEPAM of aspect ratio of 10. It can be observed that the errors remain in the same order of magnitude and bounded for most configurations. For extreme configurations (14 ≤ aspect ratio and $\Delta T \leq 15$) the error increases. In such cases, the tip loads induce greater moments on less stiff FREEPAMs thereby leading to localized kinking (configurations shown in black are configurations where FEA fails to converge). Therefore, the HSIM demonstrates length independence for cases where FREEPAMs do not undergo kinking when subjected to external loads.

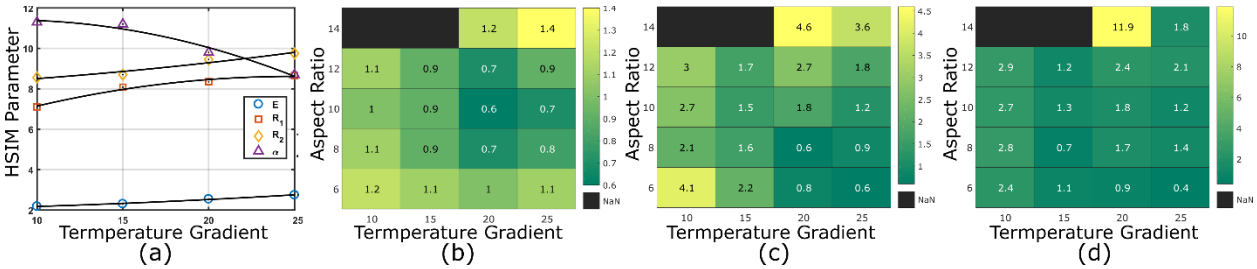

Figure 12: HSIM performance analysis (a) Variation of HSIM parameters. As the temperature gradient increases, the HSIM expands radially while keeping the thickness relatively unchanged. The stiffness of the HSIM also increases with temperature gradient while α decreases. Note: α reported has been scaled by 1e3. (b-d) Absolute error reported between FEA and HSIM for axial, bending deflections and tip slope for FREEPAMs with varying aspect ratios. Error is reported in mm and degrees.

CHAPTER 3: DESIGN AND ANALYSIS OF SOFT COMPLIANT SYSTEMS

This chapter details the utility of reduced-order models in analyzing systems of FREEs. The reduced-order models are analyzed in two paradigms: (1) As an ideation tool to explore conceptual soft architectures with superior global stroke-force properties and (2) As a synthesis tool to generate specific designs to meet prescribed requirements. Both paradigms are validated using simulations and using experimental prototypes. The analysis of mechanisms also serves as a quantitative comparison between the two reduced-order models studied in Chapter 2. From Figure 3 it can be observed that the PRBM has better accuracy and lower computation time making it the ideal candidate for analyzing planar mechanisms. However, its generalization for spatial mechanism analysis is non-trivial and encoding complex non-intuitive arrangements of FREEs can quickly become intractable. In this regard the HSIM proves useful. HSIM in conjunction with commercially available FEA solvers can be quickly used to encode complex spatial geometries and has a computation time orders of magnitude less than conventional FEA.

3.1 Investigation into Pennate Inspired Architectural Building Block

Pennation (derived from Latin “penna” meaning feather) refers to the arrangement of structural members resembling the veins and rachis of a bird feather. The presence of pennate structures is prolific in nature ranging from internal structure of algae to feathers of birds to arrangement of fibers and tendons in skeletal muscles of animals. The advantage of this arrangement is that more fibers can be bundled together in a compact volume enabling higher force generating capabilities [67]. The angle at which the fibers are inclined is termed as the ``pennate angle''. The implications of the pennate angle are significant for describing the force-stroke generating capabilities of a pennate structure. Towards capturing relevant trends, a pennate dyadic building block is analyzed as follows.

A pennate building block (PBB) in its simplest form consists of two force generating elements coupled at one end and anchored to a fixed ground at the other ends (Figure 13a). FREEs act as force generating members that mimic the effects of muscle fibers. These are similar in operating principle to McKibben muscles or pneumatic artificial muscles. The PBB enables transverse stroke generation due to constraints imposed on the FREEs during pneumatic actuation. The ratio of the transverse strain of the PBB to the axial strain of constituents FREEs is termed as the "Architectural-Gear-Ratio" (AGR). The functional dependency of the AGR with the pennation angle θ) was documented by the authors in [32]. The AGR was found to initially increase and then decrease with increase in the pennation angle θ. The maximum values of AGR was also found to be dependent on the type of joints between different elements. A configuration with pin joints was found to have a larger AGR compared to one with fixed joints. Intuitively, this arises because of variation in stiffness of the two types of joints. The type of joints being used would depend on the application and ease of manufacturability. Lastly, the AGR also affects the force generating capability of a PBB. Lower pennation angles enable larger force generation as compared to larger pennation angles. For a PBB with pin joints and pennation angle θ the net transverse force is given by the following equations

$$f_a = \pi P\{\frac{D_o^2}{4}(3cos^2\phi - 1) + [D_o t(2sin\phi - \frac{1}{sin\phi}) - t^2]\} \quad (12)$$

$$F_{net} = 2f_a cos\theta \quad (13)$$

where f_a is the actuation force developed by a FREE for a given input pressure P, ϕ is the symmetric fiber angle, D_o is the outer diameter of the FREE, and t is the thickness of the FREE. By leveraging θ effectively we can tailor the force-deformation behavior of a PBB from a displacement amplification mechanism to one that favors force generation.

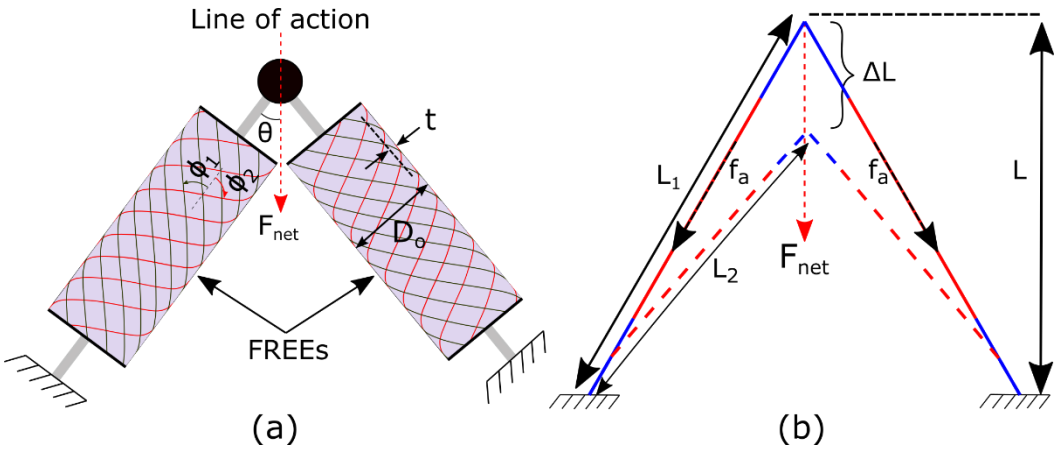

Figure 13: (a) Soft equivalent of a bipennate structure having a pennation angle θ. FREEs characterized by fiber angles (φ_1, φ_2) are used to generate contraction forces. When pressurized, transverse stroke is achieved through FREE contraction and subsequent bending, (b) Analysis of the variable architectural gear ratios (AGR) displayed by the dyadic structure for different θ [32].

The effectiveness of the PBB is highlighted when it is combined in different orientations to build architectures. Global properties of architectures are heavily influenced by the properties and relative alignment of the unit cells. In this section we analyze the effects of orientation and constraints on the global force-deformation characteristics of architectures.

Figure 14 (a, b) shows two possible arrangements of the PBB termed as conventional and inverted pennation. The conventional pennate structure comprises of two stages that are aligned symmetrically with each end node connected to the corresponding node of the previous layer. The resultant net force enacted by the system is a linear combination of the force generated by each stage. However, the net AGR remains equal to the AGR of each stage. The inverted pennate structure has two stages with the second stage being a mirror of the first stage. The two stages are constrained at two ends with one end left floating. The resulting displacement can be determined by free-body mechanics (Figure 14b).

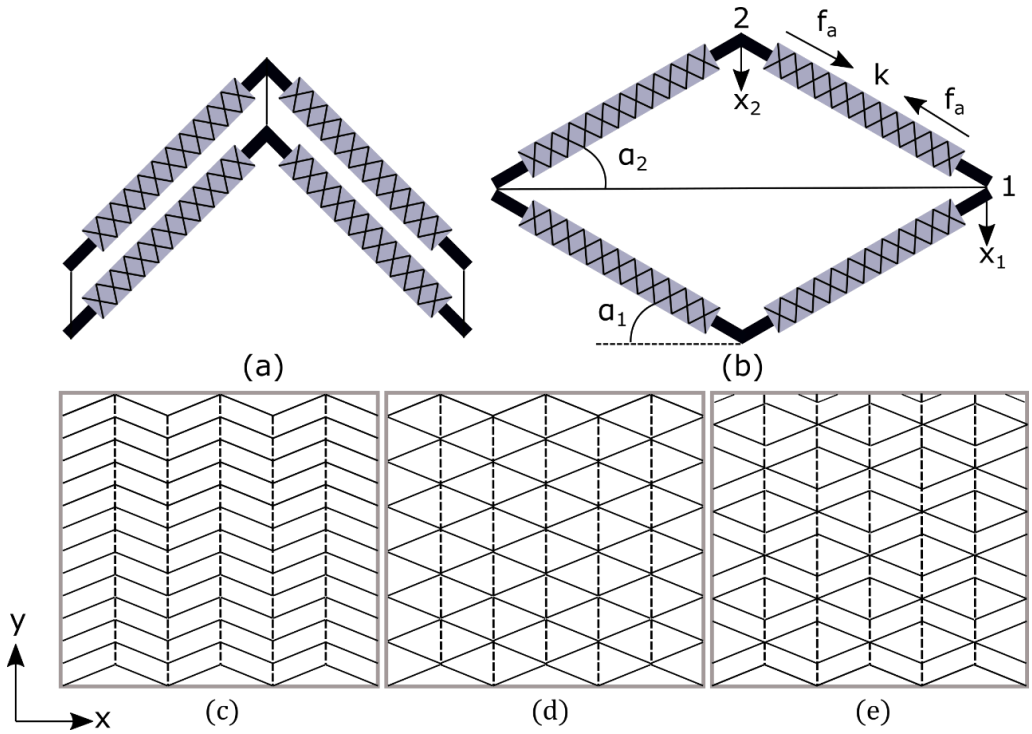

Figure 14: (a) Conventional pennation that enforces a constant AGR with amplification of net force as a function of number of layers, (b) Inverted pennation that causes an amplification of net displacement as a function of number of layers while keeping net force and (c-e) Variations of possible architectures obtained by combining the two forms of the PBB.

Each FREE is approximated as a linear spring subjected to an actuation for *fa* and with a linear stiffness *k*. This assumption remains valid from results reported in [32]. We assume no bending to occur as the joints are pinned. Applying force balance along the direction of stroke at points 1 and 2, we obtain the following equations:

$$f_a sin\alpha_2 - k(x_2 - x_1)sin\alpha_2 - f_a sin\alpha_1 + kx_1 sin\alpha_1 = 0 \quad (14)$$

$$-f_a + k(x_2 - x_1) = 0 \quad (15)$$

For $\alpha_1 = \alpha_2$, we obtain $x_2 = 2x_1$. Therefore, the net AGR is a function of the number of layers in the network while the net force equals the force exerted by each stage. For a network with *n* rows and

m columns (Figure 14 (c-e)), the global characteristics are tabulated in Table 5. Note: For the same design space the effective number of rows for a hybrid network *n'* is less than that for the inverted pennate network. The performance of architectures also depends on the positioning of constraints. A planar architecture with no constraints would force each PBB to contract along both *x* and *y* axes uniformly. This would cause the network to shrink. To obtain ARG > 1, the anchor points in the PBB are constrained to prevent deflections along *x* axis which forces the network to deform by a greater magnitude along *y* axis. For symmetrical networks this corresponds to rigidly fixing the left and right edges of the network. For asymmetric networks care needs to be taken to ensure proper constraining to get effective displacements on the global scale. To highlight the importance of orientation and constraints two prototypes are presented and experimentally validated in the following sections.

Table 5: AGR and Fnet for different networks

Configuration	**AGR_{net}**	**F_{net}**
Conventional	1	nm
Inverted	n	m
Hybrid	n'	2m

3.2 Case Studies

This section details the effectiveness of surrogate models in capturing the quasi-static behavior of applications that incorporate FREPAMs as part of their structural makeup and drive mechanism. The first case study presents the design and analysis of a compliant gripper actuated by a dyad configuration of FREEs. Analysis of the dyad structure is presented in [32] and the salient features of such an arrangement are as follows. As shown in Figure 15 it is observed that the stroke generated

increases with the pennation angle up to a threshold value (of x ≈ 22°) and then decreases. Concurrently, the actuation force generated at B increases nonlinearly with pennate angle and reaches a maximum value at x = 90 °. The studies concluded that the dyad topology of FREEs can be used effectively as building blocks for soft robots, as it can modulate between high stroke-low force and low stroke-large force scenarios by varying the pennate angle. The gripper body comprises of two slender 3D printed ABS beams, and a driving mechanism is composed of dyad FREEs inclined at a desired pennate angle (q). Analysis of the entire gripper involves modeling both the FREEs and the ABS beams using the PRB parameters. The PRB model for the beam uses two torsional springs, but with a rigid member instead of a linear spring implying large axial stiffness, and no actuation force implying passive deformation. The kinematic analysis involves using a symmetric half of the gripper is considered, which is further bifurcated into two loops 1 and 2 as shown in Figure 13 leading to end points A and B. The bifurcation is required because the FREE and the ABS gripper constitute a parallel mechanism, which are analyzed independently. We formulate the kinematic loop closure equations [68] to obtain the co-ordinates of points A and B as a function of internal deflection parameters. The coordinates can then be expressed as a nonlinear function of the PRB angles using forward kinematics.

$$x = f(q) \tag{16}$$

$$\delta x = J\delta(q) \tag{17}$$

where x = (x_A;y_A;x_B;y_B), q = (q_1;q_2;dl;q_3;q_4;q_5;q_6) and J is the jacobian matrix. The first three parameters characterized the deformation of the FREE, while the last four characterize the deformation of the beam.

Virtual Work Formulation: The virtual work equation is written for both loops separately with the external forces acting in loop 1 are Fx_A to constraint point A along y-direction, and reaction Fy

exerted by the ABS members to resist downward deformation. Similarly, the external forces acting in loop 2 are Fx_B exerted to constraint point B along y-direction, and a downward force Fy felt by the ABS members that seek to pull point B downward. We note that the force Fy is an internal force and thus acts in the opposite direction for both loops.

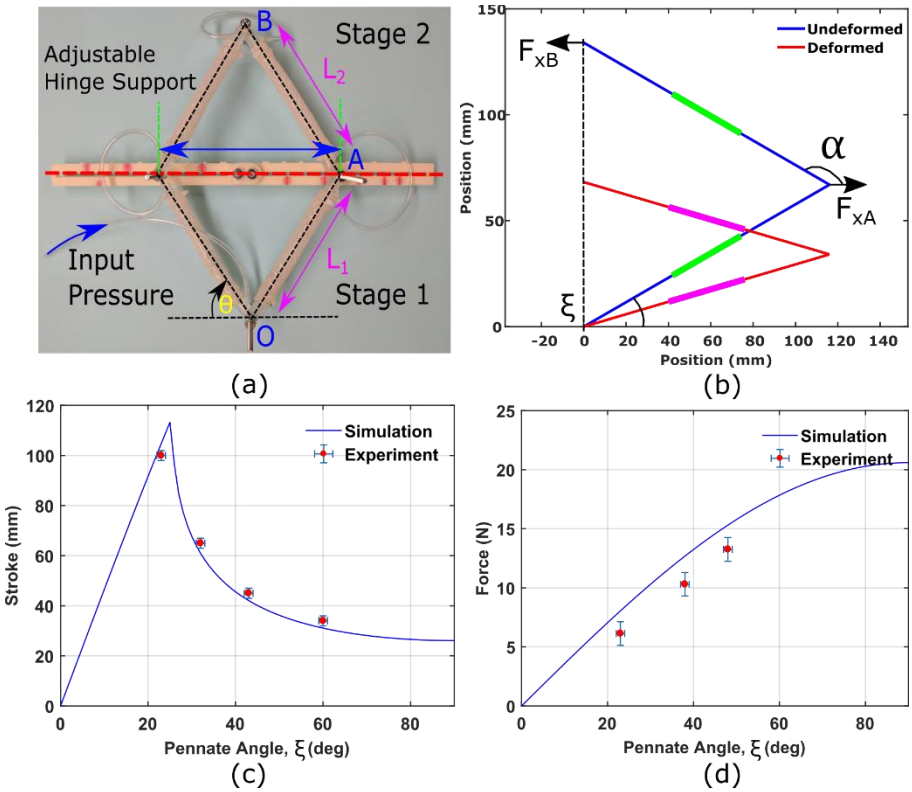

Figure 15: (a) Prototype, (b) PRB model of two-stage pennate arrangement showing the deformed configuration when FREEs are pressurized, and Study of variation in (c) transverse stroke and (d) force generated with pennate angle for fixed actuation pressure

Numerical Solution: The virtual work equations are numerically solved along with the following kinematic constraints that equate the displacements of points A and B.

$$x_A - x_{initial} = 0$$

$$x_B - x_{initial} = 0$$

$$y_A - y_B = 0 \qquad (18)$$

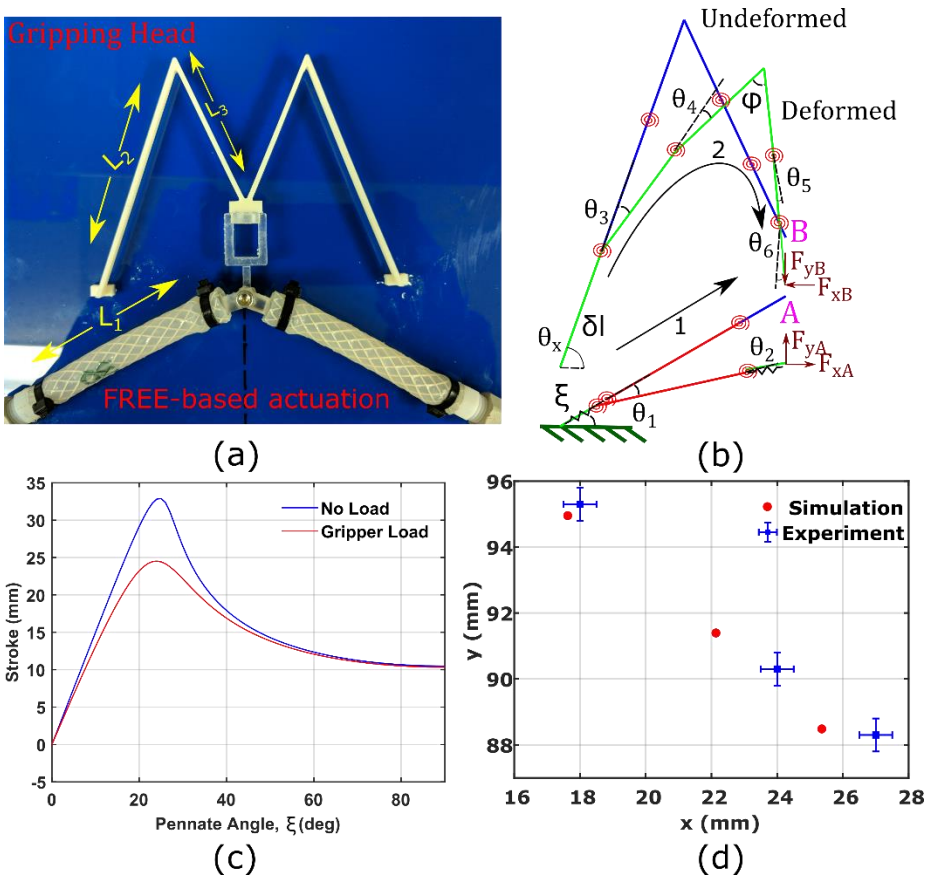

Figure 16: (a) Compliant Gripper prototype, (b) PRB model for the gripper. Variation of (c) stroke and (d) force of compliant gripper with pennation angle.

Results from this analysis is shown in Figure 16. We first determine the optimum pennate angle that leads to maximum stroke. We observe that the stroke is maximum at around x = 30°. To validate the analysis, a prototype was constructed with x = 30°. Each half of the gripper is comprised of two beams made from ABS plus plastic (E=2200 MPa). Bending characteristics of the beams are captured using the same PRB model approximation from FEA. Next, we compare

the deformed coordinates of the gripper tip from PRB model and experiment. Experimental results presented a maximum error of 1.85 mm and 1.08 mm along the x and y axis respectively.

The second case study presents a soft rotary motor concept. The presence of rotary servomotors is almost ubiquitous in modern day industries. Lightweight motors with large load torque are particularly attractive for aerospace applications like deployment mechanisms used in solar arrays and antenna drives. In this section, we design a rotary motor to maximize its angular displacement by optimal placement of the FREEs. The proposed concept is shown in Figure 17. The design comprises of a central rotor assembly that is connected to four symmetrically distributed FREEs. The FREEs act as actuating members and when pressurized they bend and provide torque and angular displacement (θ_m) at the rotor. Furthermore, the angular displacement is a function of the pennation angle (α) at which the FREEs are connected to the rotor. Each FREE connected to the rotor has four joint variables q = (q_1; q_2; dl; q_3) and two forces F = (Fx; Fy) working to keep the tip position of the floating link fixed. Four constraints are obtained from the virtual work formulation and the remaining two from Eq. 19. The rotor angle is calculated as: θ_m=90 – (θ_{1+} θ_{2+} θ_3).

$$x_{init} - x_{final} = 0$$
$$y_{init} - y_{final} = 0 \quad (19)$$

Figure 18 illustrates the effect of pennation angle on the angular displacement. It is observed that the angular displacement increases with increase in pennation angle and then decreases beyond a threshold. The maximum value of θ_m is 48^o for ζ = 27^o at Pa = 20 psi. Figure 18 also shows a comparison between results obtained from analysis and experiments for two pennation angles, ζ =0^o, 30^o. It can be observed that the error is greater at lower pressures (< 15psi). In addition to inaccuracies present in any prototype due to geometrical faults, this error can be attributed to the configuration being present outside the testing manifold from which data was collected. As

reported earlier, the error for such points is usually larger compared to interpolated points within the test manifold. However, at higher pressures these errors reduce as the operating configuration transitions to within the test manifold.

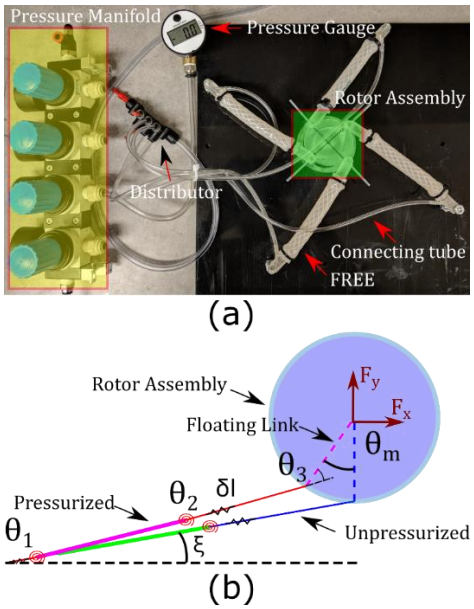

Figure 17: Soft rotary motor concept: (a) Prototype of the rotary motor, and (b) analysis model of the rotary motor with one FREE.

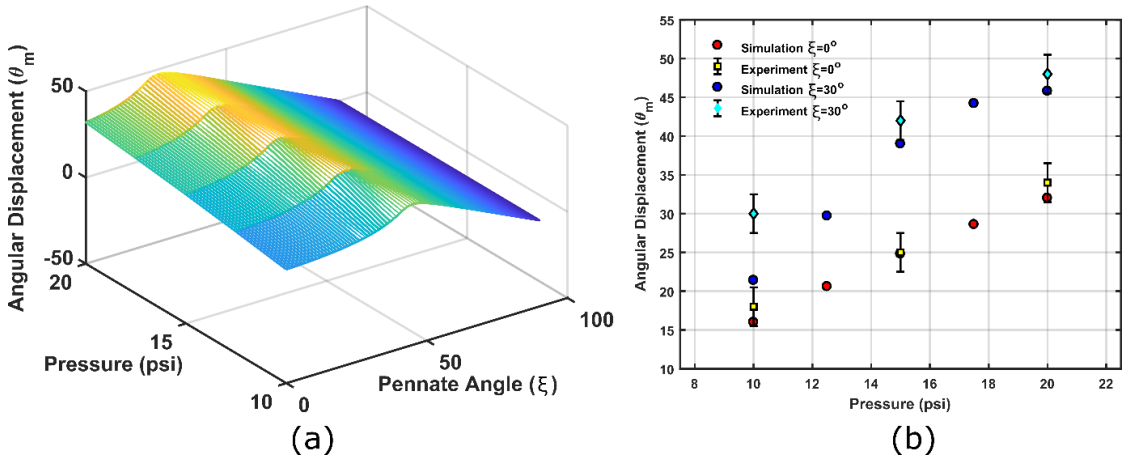

Figure 18: Performance characteristics of the soft rotary motor: (a) Variation of the maximum angular rotation with pennate angle and pressure, and (b) angular rotation as a function of applied pressure for two pennate angles.

Figure 19 details the prototypes created for the second validation study. Each prototype comprises of six FREEPAMs that have been joined at a specific pennate angle ($\theta=60^o$ for prototype 1 and $\theta=45^o$ for prototype 2). The FREEPAMs are made from latex with a fiber angle of 30^o. The joints between member FREEPAMs are kept fixed and does not allow rotation. Without constraints the base FREEPAM structure would contract both longitudinally and radially when pressurized. Therefore, placement of constraints becomes important. The first prototype is designed to amplify linear stroke and to achieve this the radial deflection must be constrained. The constraints are enforced by compliant beams placed in the interior of the soft helix shell, which ensures no radial deformations. The second prototype is designed to enable radial compression, and this is achieved by fixing both ends of the helix shell to ensure no axial deformation occurs.

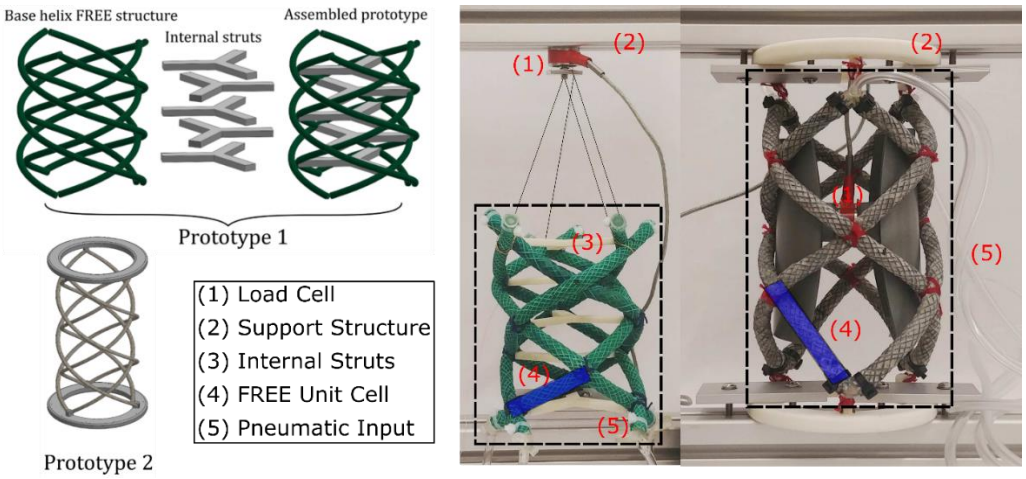

Figure 19: CAD rendering of prototype pennate networks (left) and corresponding experimental setups (right). Both prototypes are made from latex and can be structures made by arranging unit cells (highlighted) in a cylindrical fashion. Prototype 1 has a pennation angle = 60 deg and represents a stroke amplification mechanism. Radial deformation is constrained using 3D printed constraints embedded within the network. Prototype 2 has a pennation angle = 45 deg and represents a compression sleeve. Longitudinal deformation is constrained using external supports.

Each prototype can be assumed to be made from smaller unit cell FREEPAMs highlighted in Figure 19. The parameters for the corresponding HSIM for a unit cell FREEPAM are shown in Figure 20(c). It can be observed that the parametric variation is markedly different from that of the silicone FREEPAMs. Increase in stiffness with temperature gradient is capture by R_1 while the other parameters remain constant. The unit cell FREEPAMs are thinner than the silicone FREEPAMs which makes activation pressure (pressure that induces stiffness) lower. Any increase in stiffness with increase in pressure is captured by an increasing R_1 as shown in Figure 20c.

Using this HSIM model the pennate inspired architectures were modeled in ABAQUS (Figure 20d). Figure 20(e-h) details the results from the HSIM analysis and experiments. The axial displacement and blocked force of prototype 1 is presented in Figure 20(e). The prototype has an effective length of 110 mm and can generate a maximum blocked force of 29.33 N in tension and a maximum axial contraction of 30 mm (27.2 % contraction) when actuated at 30 psi (206.8 kPa). In comparison, a single contracting linear FREEPAM with an effective height of 115 mm tested in the same experiment only exhibits a maximum stroke of 10 mm at 30 psi (206.8 kPa), less than 10 % of its total length. The amplification of the linear stroke utilizing the pennate structure improves the actuation performance of miniaturized FREEPAMs. Prior work in this context has indicated that the force-stroke performance of FREEPAMs degrade rapidly with miniaturization [69]. This makes miniaturized FREEPAMs unsuitable for practical applications if arranged empirically without special considerations. However, by arranging them in a deliberate manner as in the case with the pennate structures, miniaturized FREEPAMs can be deployed effectively. The HSIM model can capture the deformation and force characteristics of prototype 1 effectively and reports an error of 1.24±1.45 mm (≈ 4.1 % error) for axial stroke and 3.99±1.92 N (≈ 13.6 % error) for blocked force. Prototype 2 reports an error of 1.49±1.01 mm (≈14.6 % error) in radial

compressive stroke and 4.27±4.35 N (≈ 6.8 % error) in net compressive force. Errors can be attributed to material property estimation during initial data collection from a high fidelity FEA simulation, the variation in the fiber angles of the constituent FREEPAMs of the prototypes and friction in the pinned joints of the test rig.

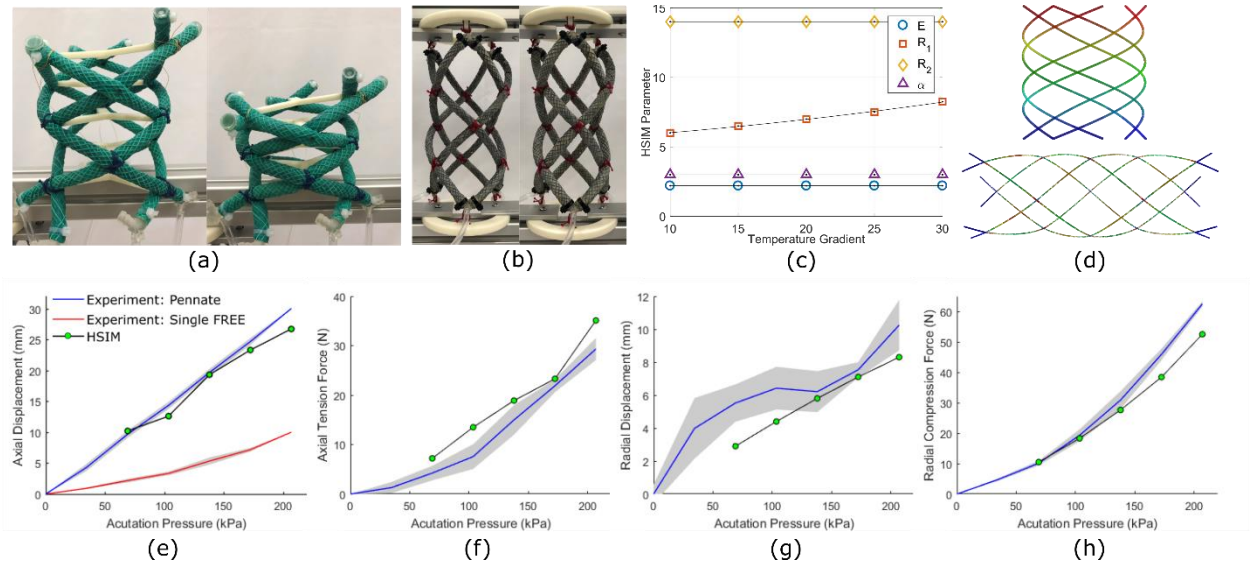

Figure 20: (a-b) Deformed configurations of prototype 1 (longitudinal) and prototype 2 (radial). (c) HSIM parametric variations with temperature gradient. Note: Results indicate a linear trend within the operating actuation input range for latex FREEPAMs. (d) Deformed configurations from FEA. (e-h) Comparison of stroke and force obtained from experiments and HSIM for both prototypes.

3.3 Surrogate Models as applied to Design Ideation

HSIM introduced in Section 2.2 can be used as a conceptual design tool for soft robots, where designers can sketch different FREE architectures and quickly evaluate potential solutions. Pneumatically actuated soft robots generate spatial motions due to constrained inflation of elastomeric chambers. The constraints are induced through strain limiting layers with higher

stiffness than the elastomers. Thus, we envisage soft mechanisms as a network architecture of FREEPAMs and strain limiting constraints. The strain limiting constraints are considered as compliant beams that can take axial and compressive loads. We believe this tool will form the basis of formulating guidelines to systematically design soft mechanisms as a combination of FREEPAMs and constraint members in the future.

The first example shown in Figure 21 is a tip-tilt stage driven by six FREEPAMs of length 130 mm.

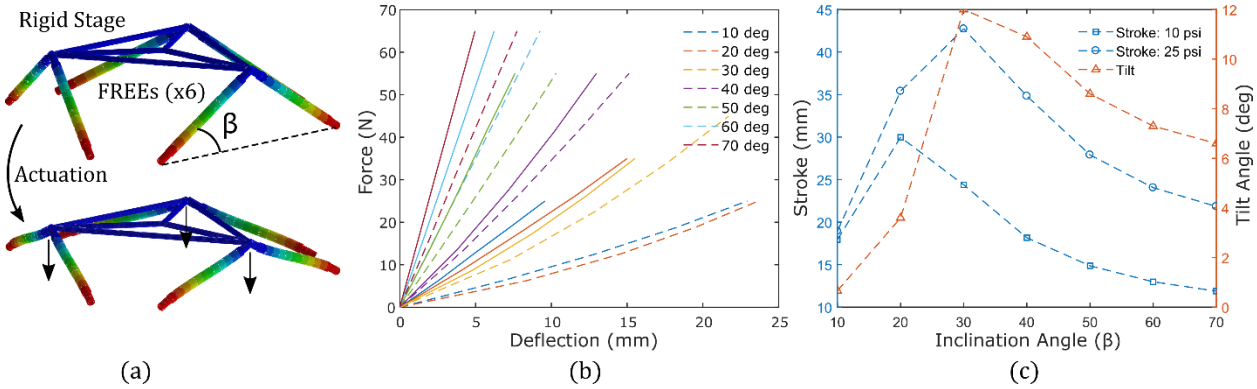

Figure 21: (a) HSIM analysis of soft tip-tilt platform concept. (b) Variation in stiffness of the platform and (c) Variation in maximum stroke and tilt angle as a function of inclination angle (β). Note: βc is the inclination angle corresponding to maximum axial

The FREEPAMs are connected to the rigid stage by using fixed joints for this analysis. By differentially actuating the FREEPAMs, the rigid stage is capable of different modes of deformation, such as axial translation and bending and constitute a 3 degrees of freedom system. The FREEPAMs are limited to operate between 10.0-20.0 psi (0.069-0.014 MPa). The rigid stage translates axially when all the FREEPAMs are actuated to the same pressure and tilts when the actuation pressures differ. The platform is capable of a maximum axial stroke of ~ 44 mm and a

tilt angle of ~ 12 deg. The axial deformation trend is in agreement with results reported by the authors in [32]. The next parameter of importance for the stable operation of the stage is its stiffness, or its ability to resist external loads. Figure 21(b) shows that the stiffness of the stage depends on the inclination angle, β, where a decrease was reported for $\beta \leq \beta_c$ and an increase thereafter. The indicates an indirect relation between stiffness and axial stroke generated by the FREEPAMS. In Figure 22, we present more examples of spatial soft mechanisms obtained using three dimensional combinations pennate building blocks. These designs were validated using the HSIM model in ABAQUS.

- Soft Compliant Bending Member: Design 1 shown in Figure 21(a) represents a concept of a bending mechanism with possible applications in designing a gripping finger. HSIM is used to design the cross section of a finger such that on when actuated the finger bends and curls around the object like pneunets [70]. The gripper comprises of two sections that generate differential stiffness when the network is actuated. The compliant section consists of six PBBs arranged to generate large axial (downward) stroke. The stiffer section (highlighted) has compliant beams running along its length from the ground up and the three and a half PBBs in this section are oriented to generate no axial stroke. The interaction between the two sections induce a moment at the tip of the gripper which forces the overall network to bend. For a predefined actuation pressure, the curvature of bending remains a function of the number of PBBs in each section and the stiffness of the struts. The gripper has an effective length of 528 mm and the tip displaces 295 mm along the x-axis and 79 mm along the y-axis and produces a total blocked gripping force of ~ 26 N.
- Shape Morphing Wheel: Design 2 shown in Figure 21(b) represents a concept for a soft shape morphing wheel that could have potential applications in space exploration

specifically planetary rovers. Shape morphing becomes important as it can be used to modulate the area of contact with the terrain thereby adjusting amount of traction. A larger surface area is suited for sandy/soft terrain while rougher/harder terrain requires lower traction. The presented design is radially symmetrical with a central axle mount. The surface of the wheel has two type of control points: (1) load bearing points and (2) maximum deflection points. The load bearing points are connected to the axle mount through struts while the maximum deflection points are incorporated into PBBs. The soft wheel is designed to operate in two conditions: (1) When unactuated the wheel conforms to a triangle with very low stiffness. In effect, this configuration mimics a soft outer track supported on an internal stiffer skeleton thereby increasing the area of contact with any surface. (2) When actuated the wheel conforms to a stiffer hexagonal configuration that has a radius equal to the incircle of the unactuated configuration. The area of contact is reduced which reduces rolling resistance for harder terrain. The unactuated wheel has a radius of 420 mm and actuated configuration has a radius of 280 mm. Assuming constant thickness, the line of contact reduces from 485 mm to 314 mm (35.3 % reduction). The design is evaluated for its load bearing capability in the actuated configuration. An axle load of 20 N acting downwards does not displace axle mount when the load bearing points are in contact with the ground and displaces axle mount by 95 mm when the maximum deflection points are in contact with the ground. When unactuated and loaded, the FREEPAMs undergo kinking making analysis unstable and beyond the scope of this framework.

- Spiral Gripper: Design 3 shown in Figure 22(c) represents a concept for a scaled up spiral gripper suited for grasping and manipulating long slender objects in low gravity

environments like space or marine environments. The spiral gripper has a modular design with unit cells stacked along the axis of the gripper and incrementally offset at an angle. The gripper has 36-unit cells each of which is incrementally offset by 10 deg. Each unit cell comprises of eight FREEPAMs that are joined at one end and mounted on rigid circular rings on the other end. The FREEPAMs configuration is skewed such that one half of the FREEPAMs are positioned at a steeper angle (60 deg) than the other half (30 deg). The rigid rings are also connected by means two parallel compliant beams that bend and two compliant dyads that compress. On actuation the FREEPAMs induce a moment on the upper stage and causes upper ring to tilt. The HSIM reports a tilt of ~ 9.5 deg. The combined effect of localized bending of each unit cell and the angular offset between consecutive unit cells manifests as a global spiral motion that wraps around a body parallel to the undeformed gripper axis. The curvature of the spiral is a function of the bending of each unit cell and angular offset between unit cells.

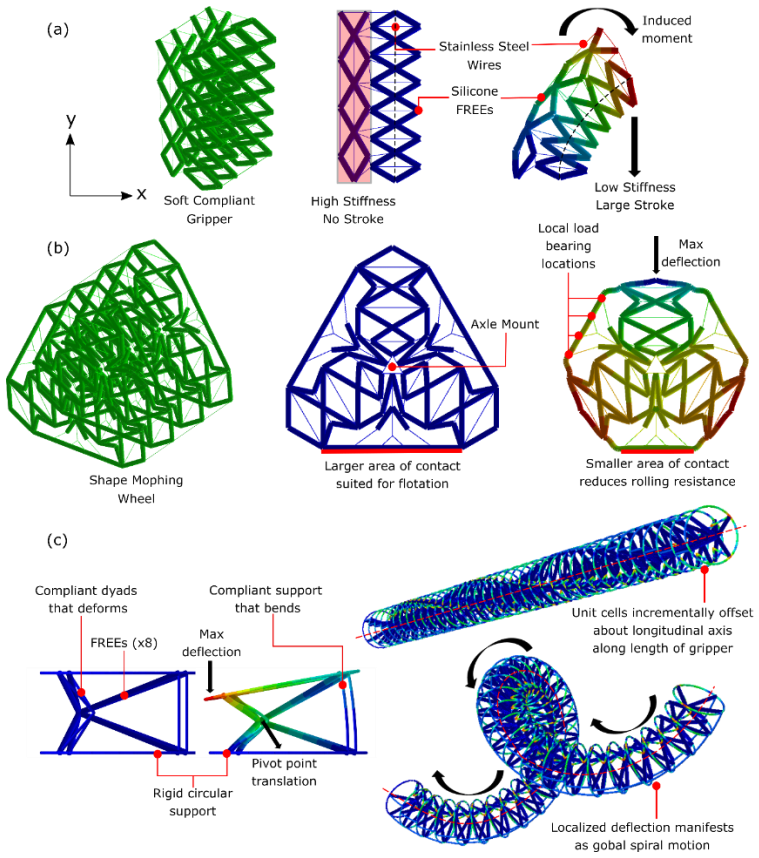

Figure 22: Exploration of design concepts based on soft compliant architectures. (a) A scaled up soft gripping finger that bends when actuated. FREEPAMs generate required force and stroke while the compliant constraints transmit compressive loads and are used to change local stiffness of the structure based on orientation. (b) Shape morphing wheel comprising of a compliant skeletal structure with load bearing spokes emanating from a central axle mount. FREEPAMs are embedded to maximize stroke and force at select regions. The wheel is designed to function in hard and soft terrains. (c) Spiral gripper made from unit cells stacked and offsetted about the longitudinal axis. The unit cell bends locally due to differential stiffness and this manifests as a global spiral motion. Such grippers are suited for grasping long slender bodies like an elephant's trunk

3.4 Surrogate Models as applied to Design Synthesis

Efforts to integrate actuation and transmission gained significant attention from the compliant mechanism community, where embedding actuators in a network of compliant members was sought. To understand the performance benefits of embedding actuators within the mechanism topology, consider the example of a compliant inverter shown in Figure 23(a), where the force and displacement of the contracting actuator at the input is inverted at the output. While the actuator type can be generic, we consider a soft Pneumatic Artificial Muscle (PAMs) [71] in this example because of its inherent flexibility. As with most actuators, the force produced depends on the pressure and the diameter, while the net stroke depends on the length. In the first case of Figure 23(a), the entire actuator length (L_{eff}) is lumped at the input and the measured force-deflection plot of the system is denoted in Figure 23(c) (red squares). In Figure 23(b), certain compliant members are replaced by the actuators and the resulting stroke of the system (blue lines in Figure 23(c)) has increased, while keeping the forces constant. Thus, strategically embedding flexible or soft actuators within the compliant topology may increase output stroke by reducing the net passive stiffness, while still maintaining the kinematic leverage and output forces.

The presented approach involves first following the previously established guidelines to design compliant mechanisms and then replacing certain compliant members with contracting actuators. This can be a complex process because identifying the exact members to be replaced without changing the kinematic behavior is non-intuitive. An overview of the load flow framework to design compliant mechanisms is presented and then systematically formalize design guidelines to embed actuators.

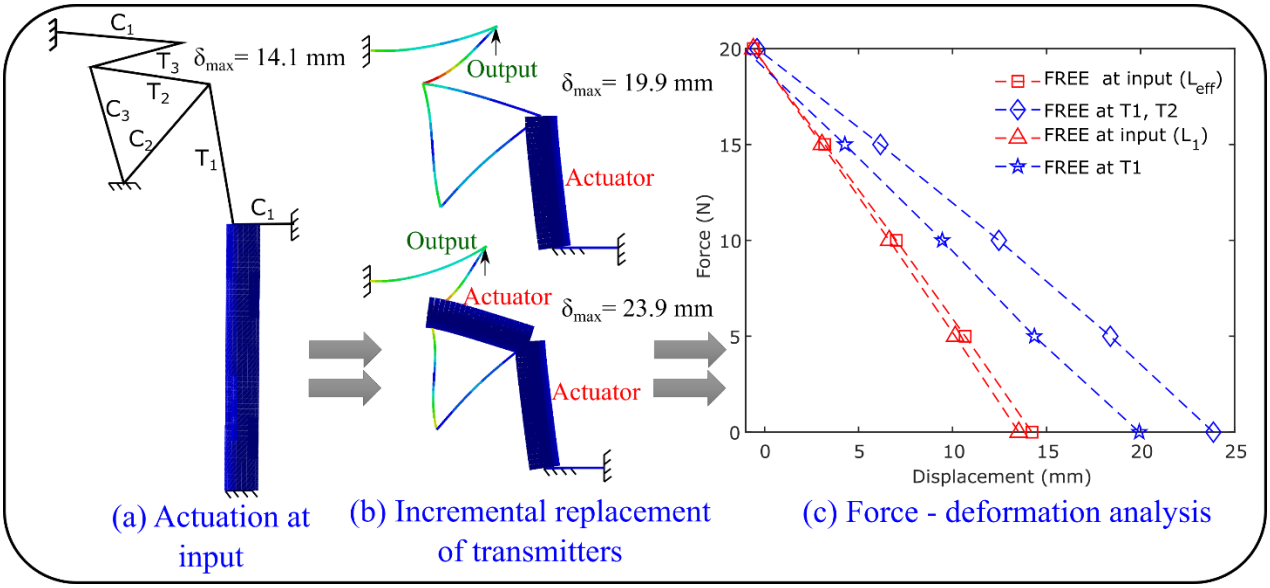

Figure 23: Benefits of distributed actuation versus concentrated actuation at input in a compliant mechanism. (a) An inverter mechanism with an actuator mounted at the input compared against (b) distributed actuation schemes where transmitters are replaced according to certain design guidelines. (c) Effectiveness of the modified mechanism is analyzed to assess if requirements are met. Mechanisms with embedded actuators are observed to generate larger strokes compared to the base mechanism being driven by an actuator of the same volume at the input.

3.4.1 Load Flow Visualization

Load flow is vector field of fictitious forces that flow through the mechanism geometry from input to output. These fictitious forces called “transferred loads” can be quantified using the compliance matrices that relate forces and displacement between any two points in the topology as detailed in [72], [73]. Load flow enables functional characterization of the mechanism geometry into transmitters and constraints. A member with a predominantly axial load flow is called a transmitter, while a member with transverse load flow and moment components can be called a constraint. This framework can be used to analyze a mechanism by decomposing it into building blocks of transmitter-constraint sets. The decomposition of a compliant mechanism topology based

on load flow into transmitters and constraints can be inverted for conceptual design synthesis. This was demonstrated for the design of compliant metamaterials and spatial - compliant and shape morphing mechanisms in [74].

3.4.2 Actuator Model

While the presented framework is applicable to both extending and contracting actuators, the presented study is limited to contracting actuators - specifically contracting Fiber-Reinforced Pneumatic Artificial Muscles (FRPAMs). FRPAMs are a class of pneumatic actuators that are composed of a soft elastomer shell reinforced by inextensible fibers that govern the mode of deformation. In this work, FRPAM deformation is captured using HSIM approximation. Each FRPAM is characterized for a specific actuation pressure and analysis is carried out to match the axial and bending stiffness of the FRPAM with that of a nonlinear beam. Data for FRPAM deformation is obtained using FEA. For the presented analysis, FRPAMs with a fiber angle, $\alpha = 30^{o}$ and pressurized to 172.369 kPa is used to generate a blocked force of approximately 55 N.

3.4.3 Design Guidelines

The embedding of actuators within a compliant mechanism requires the designer to adhere to certain guidelines that enables the correct selection of replacement members. The guidelines are formalized as shown in Figure 24 and detailed below:

1. *Perform load flow analysis on the base compliant mechanism to identify constraints and transmitters.*
2. *Construct connectivity graph for the mechanism and identify transmitters in tension that can be replaced using contracting actuators. Transmitters in compression are replaced when using extending actuators.*

3. *Ground the input and incrementally replace transmitters in tension with actuators till requirements are met.*

Auxiliary guidelines:

- *Transmitters with load flow that are not predominantly axial, when replaced, may negatively impact the performance of the mechanism.*
- *For mechanisms with multiple paths between the input and output, replacement occurs concurrently along each path starting from the input and terminating at the output.*
- *To ensure that the deformation geometry is maximally preserved when embedding actuators, a member along a path is replaced only if concurrent members can be replaced in each path simultaneously.*

To clarify consider Figure 24(b), which presents a connectivity graph for a compliant mechanism with transmitters in tension identified in red and the node number indicating the depth of the node within the mechanism. The mechanism has four paths connecting the input to the output and a depth of three levels. From the auxiliary guidelines replacement of transmitters in tension starts at level 1 and proceeds to level 2 along each of the available paths. This corresponds to a total replacement of five members with FRPAMs (Input→1, 1→2). However, level 3 members are not replaced as all connecting members cannot be replaced owing to two members being under compression (2→3). Therefore, the replacement stops at this level.

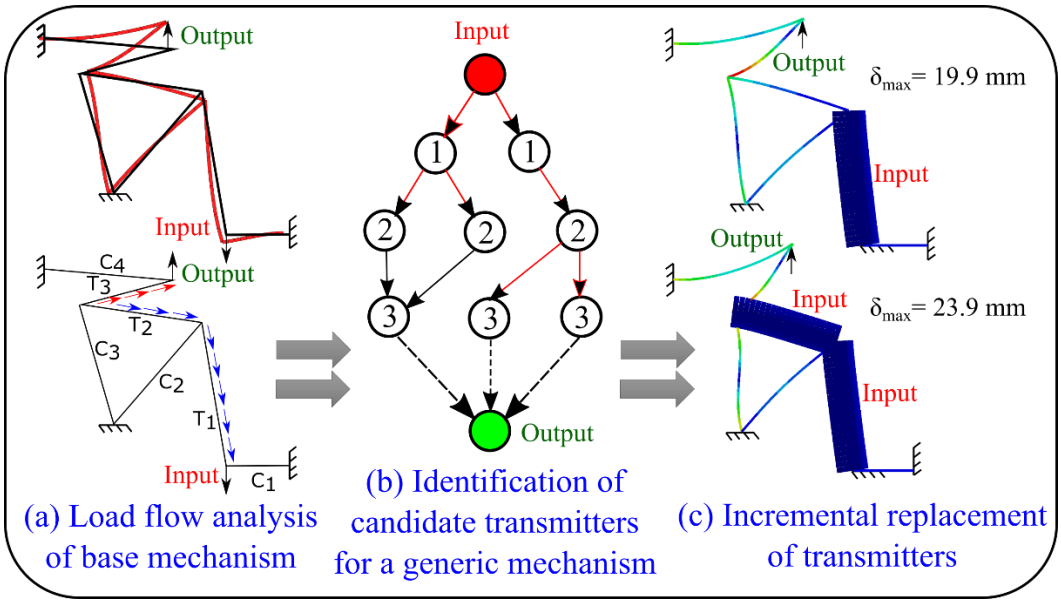

Figure 24: Design framework presented in this work. The process starts with (a) load flow analysis of the base mechanism to identify transmitters and constraints. (b) A connectivity graph is used to identify potential replacement members along each path starting at the input and terminating at the output. (c) Transmitters are replaced according to design guided lines.

3.4.4 Design Examples

The first example illustrated is an inverting compliant mechanism. The first step is to perform the load flow analysis on the base mechanism to identify the transmitters and constraints. We then construct a connectivity graph from the input to the output. From the load flow visualization and the connectivity graph shown in Figure 25(a), we can identify feasible transmitters i.e., transmitters in tension to be replaced with contracting actuators. The final step is to ground the input of the mechanism and replace the transmitters in tension with actuators. In this example, we identify three transmitters (T_1, T_2, T_3) with two of them T_1, T_2 being in tension. We replace the transmitter T_1 with a FRPAM actuator and obtain an output displacement of 26.8 mm. We then replace the next transmitter T_2 with a FRPAM actuator and obtain an increased output displacement of 29.5 mm shown in Figure 25(a). The simulations are performed in a commercial

finite element software ABAQUS. It can be observed that the mechanical performance of the mechanism has been improved with incremental replacement of transmitters with FRPAMs. Note: It is important for the designer to check for any instabilities caused by the replacement of the transmitters. For example, if the base mechanism is not sufficiently stiff, direct replacement of a transmitter with a FRPAM might lead to buckling instability which can potentially place constraints on the force-displacement relationships of the mechanism.

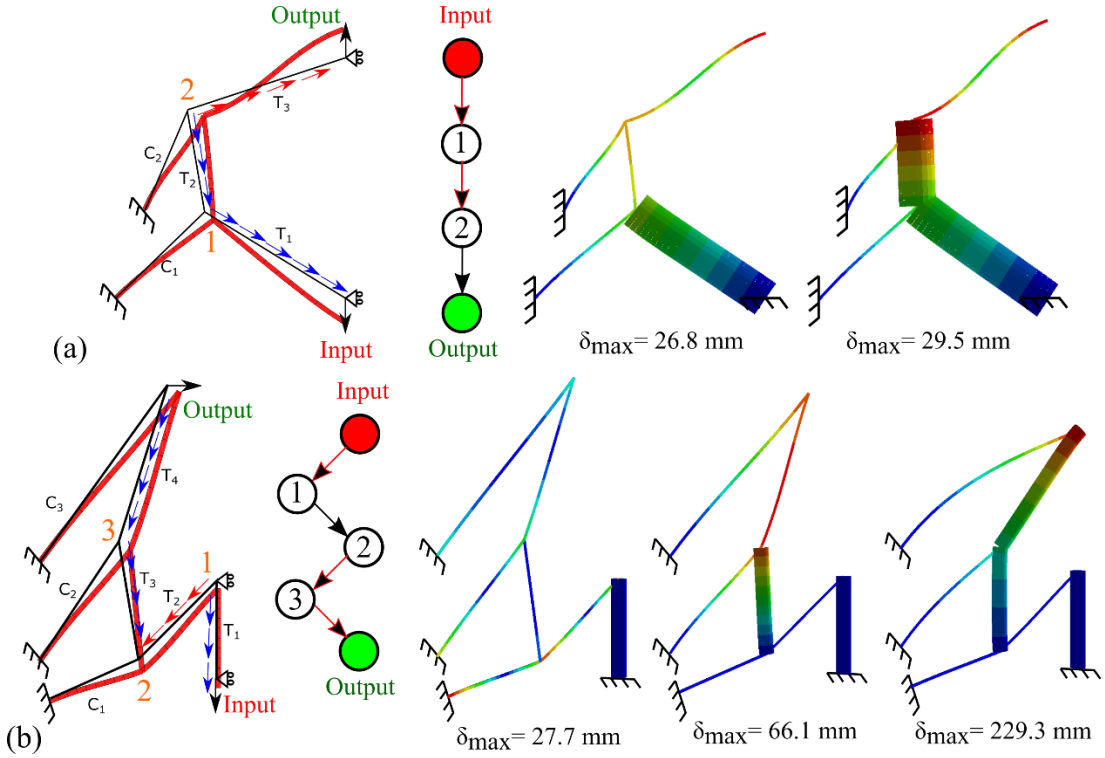

Figure 25: Simulation results. Symmetric half of (a) an inverting and (b) gripping mechanism with embedded FRPAMs. Incremental replacement of transmitters with FRPAMs increases tip displacement at the cost of increased complexity.

The second example illustrated is a compliant gripper. The load flow visualization and the connectivity graph are shown in Figure 25(b). As per the guidelines, we identify the feasible transmitters. In this example, there are four transmitters in the load path from input to output. We

observe that T_1 is in tension, while T_2 is in compression and T_3, T_4 in tension. We ground the input and the transmitters are replaced incrementally in steps. Simulations are performed after each replacement and obtain output displacements of 27.7 mm, 66.1 mm and 229.3 mm corresponding to replacement of T_1, T_1-T_3 and T_1-T_3-T_4 respectively shown in Figure (b).

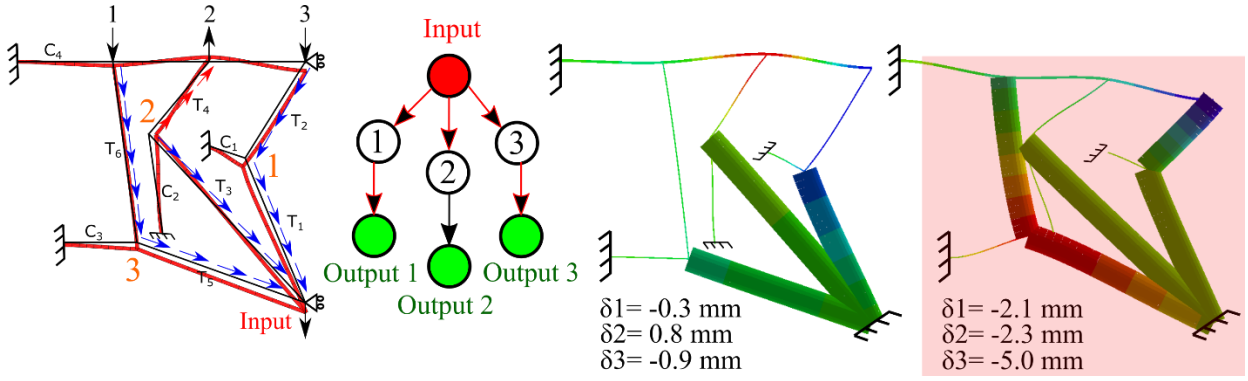

Figure 26: Simulation results for a shape morphing mechanism. Replacing the first level of transmitters generates the desired shape at the output. However, replacement of the remaining members to increase deflection results in a distorted output (highlighted). The second level of replacement violates auxiliary guideline 3.

To demonstrate the efficacy of the design framework for single-input multiple-output systems, a shape morphing example is presented and shown in Figure 26. The design requirement of the mechanism is to achieve a sinusoidal shape at the output. The load flow analysis is performed, and a connectivity graph is constructed. We observe three parallel load paths from input to each of the outputs. From the load flow visualization, we can identify that each load path from input to output has two transmitters: T_1-T_2 from input to output 1, T_3-T_4 from input to output 2, T_5-T_6 from input to output 3. From connectivity graph, we can also classify each of the transmitters to be either in tension or compression i.e., T_1, T_2, T_3, T_5 are in tension and T_4 is in compression. The mechanism has a two-level depth and as per the design guidelines the input is grounded. Since, the first level has all the transmitters of parallel load paths in tension, they can be replaced simultaneously

according to auxiliary guidelines 2-3. Transmitters T_1-T_3-T_5 are replaced and the simulations validate the performance of the mechanism. The second level of the mechanism has two transmitters in tension and one transmitter in compression and hence the second level of replacement violates auxiliary guideline 3. To showcase the validity of auxiliary guideline 3, the two transmitters in second level are replaced with actuators and we observe that the output shape of the mechanism is distorted as shown in Figure 26.

The design framework can also be extended to spatial mechanisms as illustrated using a three-dimensional (3d) gripper in Figure 27. The 3d gripper is constructed using two different mechanisms shown in Figure 27(a). Mechanism-1 converts linear translation to rotation (or couple) and mechanism-2 converts the rotation (or couple) into gripping motion (twist). Using these two mechanisms in conjunction, we construct a conceptual 3d gripper shown in Figure 27(b). Mechanism-2 is radially patterned on top of the mechanism-1 such that the input translation activates the rotation of the rigid ring and consequently the output twist of the mechanism-2 to achieve a gripping motion shown in Figure 27(c). The radially patterned mechanism-2 members twist to create a reduced circumferential space that can be used for gripping. As per the design guidelines, load flow analysis has been performed on each of the mechanisms shown in Figure 27(a) and feasible transmitters are identified. Mechanism-1 has two parallel load paths and two-level depth. All the transmitter members in this mechanism are in tension.

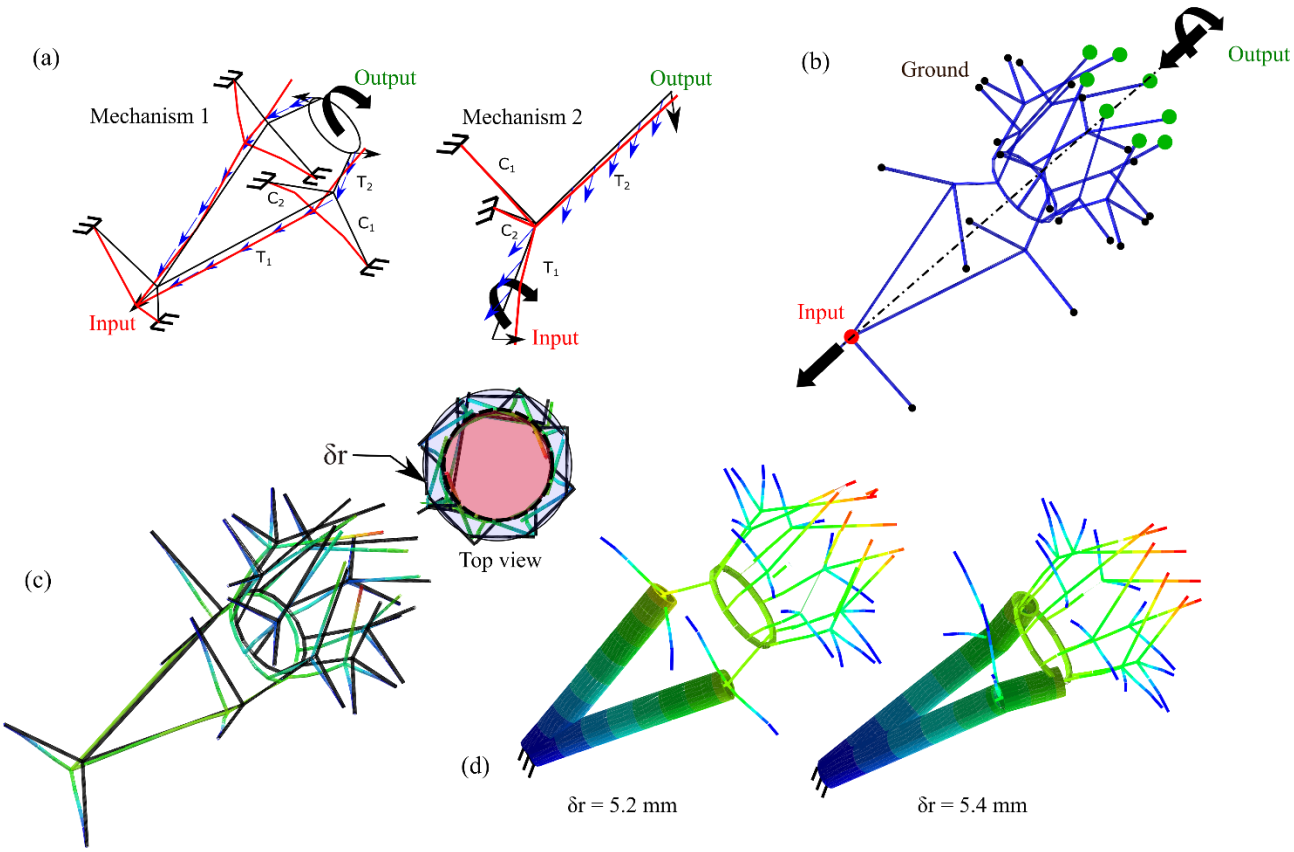

Figure 27: Simulation results for a 3D gripper. (a) Mechanism 1 converts a linear input stroke into an intermediate couple and mechanism 2 converts the intermediate couple into a twist at the output (b) Gripper morphology: The gripper comprises of two mechanisms connected by a rigid ring (c) FEA of the gripper showing reduction in circumference of the gripping head under actuation. (d) Gripper with embedded FRPAMs generating a twist at the gripping head. Note: Replacement of the second level with FRPAMs results in a minor improvement in output deflection due to small lengths of the second level FRPAMs.

The transmitters are replaced incrementally at both the levels with actuators and simulations are performed to compute the difference in the circumferential radius δr. The replacement at first level gives a δr of 5.2 mm and replacement at both levels (first and second level) gives a δr of 5.4 mm. The improvement in the δr with replacement at both levels is minor due to the smaller lengths of

the transmitters at level 2. Smaller lengths correspond to smaller strokes and consequently smaller output deflections. From observing the load flow in mechanism-2, the load flow is not predominantly axial in the transmitters. This violates the auxiliary guideline 1 and hence, the transmitters in the mechanism-2 are not replaced with FRPAMs.

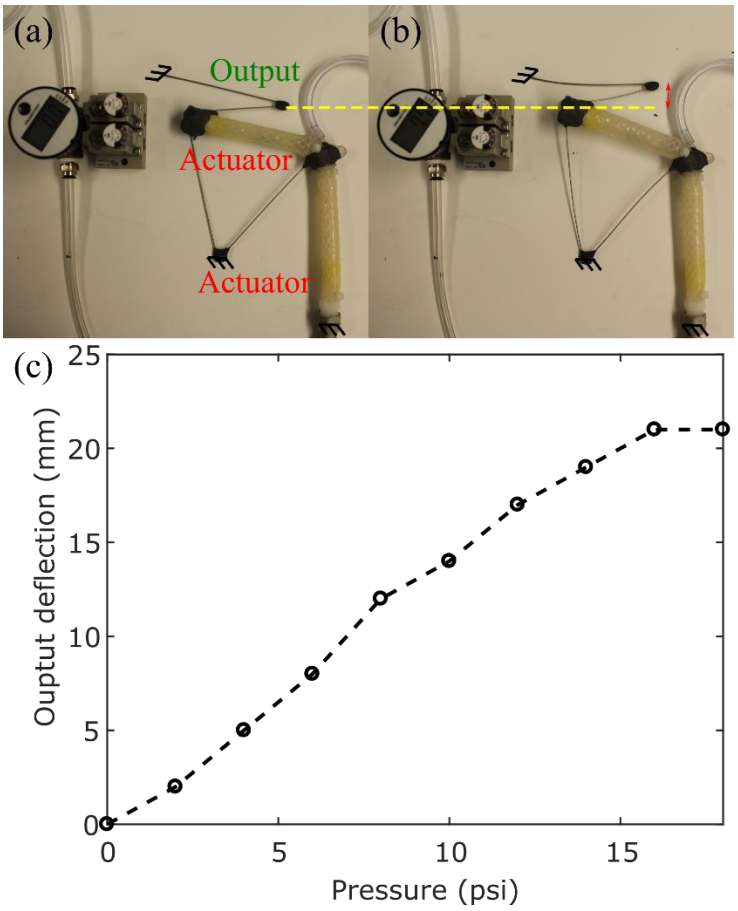

Figure 28: (a) Experimental prototype consisting of two FRPAMs embedded in an inverting compliant mechanism. (b) Deformation at 53.08 kPa (7.7 psi) and (c) Variation in output deflection with actuation pressure.

The efficacy of the design framework is also demonstrated from an experimental study on a prototype mechanism. For our analysis, we replicate the compliant inverter mechanism from Figure 23. The base mechanism is created using stainless steel wires of diameter 1 mm and

FRPAMs having an outer diameter of 13 mm and thickness of 2 mm. The joints are bonded using epoxy putty to obtain fixed joints as shown in Figure 28. The mechanism with embedded actuators is pressurized and the displacements at the output displacements are recorded. Figure 28(a, b) show the prototype before and after actuation. The variation of the output deflection with actuation pressures is plotted and shown in Figure 28(c). We can observe that the output deflection increases with the actuation pressures and at higher pressures, the variation in the output deflection is minimal.

3.4.5 Design Synthesis

Study on variation of tip force and stroke with morphology: This study explains the variation in the force exerted at the inverter tip and the stroke generated by the overall mechanism. The problem is formulated as a multi-objective optimization problem with conflicting objectives and hence it is required that a suitable pareto front is generated to study the effects of mechanism morphology on the objectives. A Non-dominated Sorting Genetic Algorithm-II (NSGA-II) [75] multi-objective routine is used in conjunction with ABAQUS FEA solver to generate the pareto frontier and HSIM is used to approximate the behavior of the embedded actuator. The pareto frontier corresponds to maximizing both the objectives simultaneously. The optimization is run for a population size of 100 for 3000 generations. The population is initialized based on empirically defined parameters. The design search space is limited by incorporating the following constraints:

1. Domain Size: The overall size of the mechanism (bounding box encompassing the mechanism) is limited to a user defined value. In our analysis, the domain size (length of each side of the bounding box) is varied in three steps: 180 mm, 270 mm and 360 mm.
2. Length of each compliant member is limited to a value between 10 mm and 270 mm.
3. Length of the FREE is limited to a value between 45 mm and 180 mm. This range corresponds to the range for which the HSIM has been validated (See Section 2.2.4).

4. The compliant members for this analysis are assumed to be steel wires having a diameter of 1.5 mm and Youngs Modulus, E = 2e5 MPa.

In this study, we report the effects that variation in domain size and morphological complexity have on the overall pareto frontier of the mechanism. Figure 29(a) presents the variation of the pareto front with size. Each pareto front presents 100 different geometries that have a combined objective value that is equal to the rest but are individually skewed to one of the objectives contingent on its location on the pareto frontier. We observe that as the domain size increases the pareto frontier is pushed further down indicating increased performance in terms of tip displacement and reaction force. This can be attributed to the design framework having access to more design morphologies and access to longer structural members as the design domain increases. FIGURE(b) showcases two extreme designs that are skewed to maximizing tip deflection and tip force.

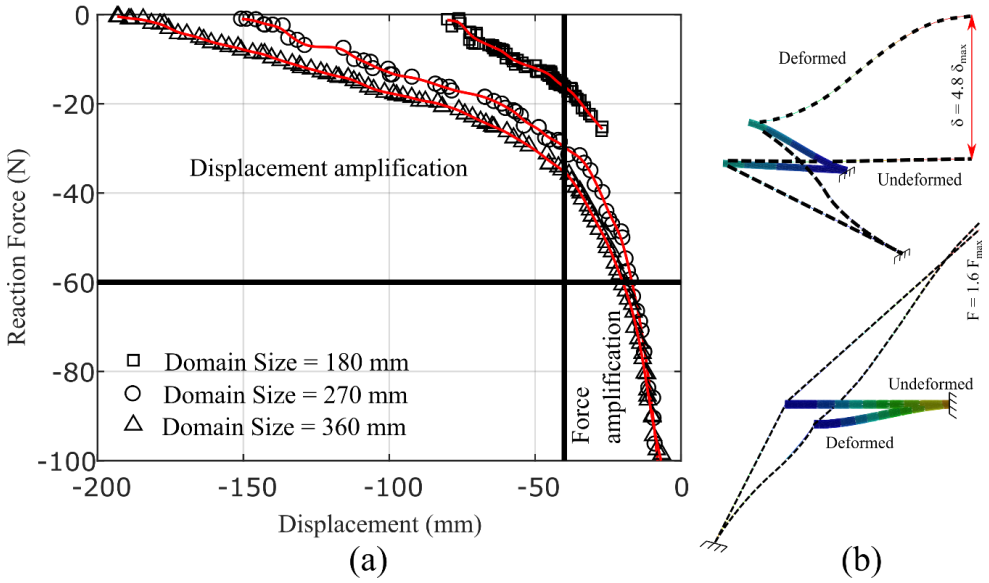

Figure 29: (a) Variation in stroke-force characteristics of inverter mechanisms with domain size. (b) Example configurations of a stroke and force amplification inverter mechanism located at the extremities of the pareto frontier.

The second study explores the effects of increasing the complexity of base mechanism. While the prior study had two compliant and one soft member (3-member), the more complex design morphology 3 compliant and 2 soft members (5-member). Figure 30 shows the variation in the pareto frontier for both morphologies with increasing effective FREE length while keeping the domain size constant. It can be observed that in each case the simpler morphology performs better especially with regard to tip deflection. This is a departure from results reported in [76] where 5-member topologies provided greater output displacement albeit with greater induced stresses. For soft compliant mechanisms with embedded actuators, distributing the actuation can affect performance due to two reasons: (1) Reduction in the net deflection exerted on the mechanism. The 5-member designs are in effect a serial arrangement of two 3-member designs each with a shortened embedded FREE. As the line of action of these FREEs are not aligned, the effective deflection of the overall mechanism will be less than that of 3-member designs. (2) Within a constrained domain having more members reduces the length of each constituent member. This affects the displacement amplification capability of certain design morphologies.

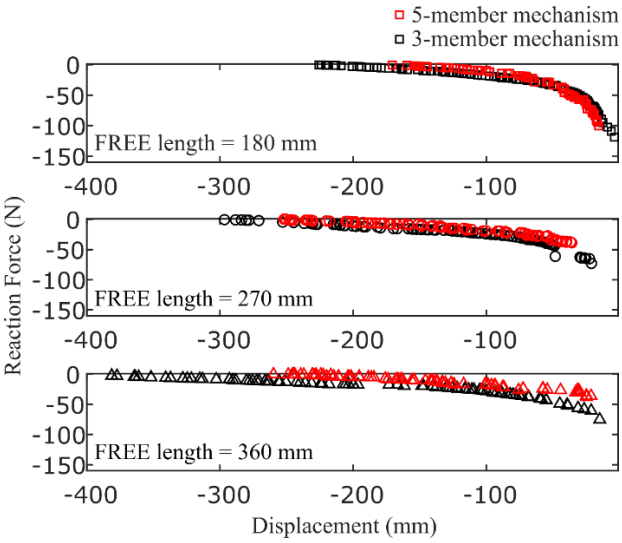

Figure 30: Variation in stroke-force characteristics of inverter mechanisms with morphological complexity and effective FREE length.

Synthesis of soft compliant shape morphing designs: This study presents results pertaining to the design of soft complaint mechanisms tailored for meeting specific deformation profiles. The design space morphology for the analysis is as follows: (1) We use three 3-member mechanisms arranged in parallel, each strongly influencing the displacement and forces at their respective control points. (2) The deformation of the control points is coupled making the design problem non-trivial. (3) The overall mechanism is constrained to a domain size of 540 mm and members should have an angular spacing of at least 10^{o}. A covariance matrix adaptation evolution strategy (CMA-ES)[77] is used to minimize the error between the mechanism deformation profile and the target deformation profile at the control points. Each design is initiated with a population size of 100 and the optimization is run for 1000 iterations. The results from the analysis are shown in Figure 31. Results for three deformation profiles evolving from the same base configuration but with different objectives are presented: (1) Concave Hull: Each mechanism exerts a varying degree of downward pulling force at each control point to obtain the desired deflection. Furthermore, the length of the embedded FREEs are varied to ensure no excess distorting force is applied at the output. An error of 2.92 mm is reported between the optimized profile and target profile. (2) Convex Hull: Exerting a pushing force derived from embedded actuators that produce a pulling force becomes non-trivial. In this example. Each mechanism evolves into an inverter thereby generating pushing forces. Each mechanism converges onto a similar morphology and scales in length to accommodate for greater output deflection requirements (left to right). An error of 4.72 mm is reported between the optimized profile and target profile. (3) Sinusoidal Hull: To generate a sinusoidal shape the control points must alternate between pulled down and pushed up while overcoming the forces exerted by the neighboring mechanisms. The final mechanism is a

combination of pull down and inverting mechanisms. An error of 4.37 mm is reported between the optimized profile and target profile.

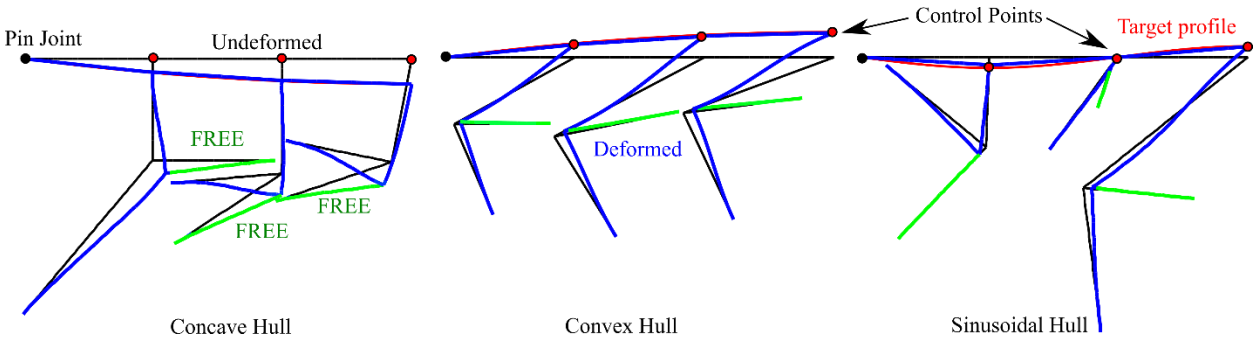

Figure 31: Design synthesis of planar soft compliant mechanisms. Each design evolves from identical initial solutions but with different objectives driving the evolution. Depending on the requirement the mechanism attached to each control point evolves into a pulling or pushing/ inverter mechanism.

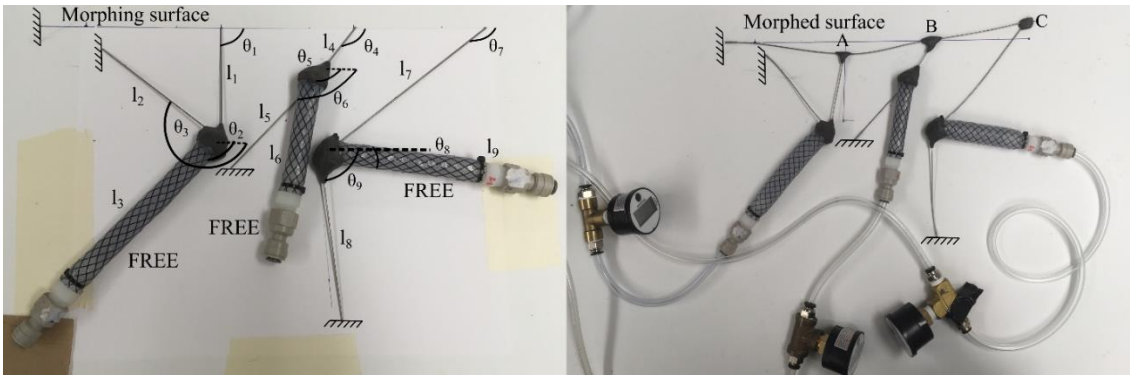

Figure 32: (a) Undeformed and (b) Deformed configurations of the planar shape morphing mechanism. The parameters of the mechanism are tabulated in

To validate the efficacy of the framework a prototype of third example design (sinusoidal hull) was fabricated as shown in Figure 32. The prototype is constructed to smaller scale with the lengths of the members being scaled and the angles remaining unchanged. As can be seen from Figure 32(b) the output takes on a sinusoidal shape albeit scaled in magnitude as compared to the

original design. A comparison between results obtained from simulation and experiments is reported in Table 7.

Table 6: Shape morphing geometry parameters

Parameter	**Value**
l_1	64 mm
l_2	90 mm
l_3	135 mm
θ_1	91 deg
θ_2	131 deg
θ_3	220 deg
l_4	20 mm
l_5	73 mm
l_6	60 mm
θ_4	126 deg
θ_5	105 deg
θ_6	131 deg
l_7	140 mm
l_8	95 mm
l_9	75 mm
θ_7	142 deg
θ_8	4 deg
θ_9	84 deg

Table 7: Displacement analysis for shape morphing mechanism

Control Point	**Simulation (mm)**	**Experiment (mm)**
A	-13	-13
B	1	0
C	18	17

CHAPTER 4: MODEL-FREE CONTROL OF A SOFT ROBOT

The BR^2 manipulator presented in [9], is a continuum robotic arm made from combining soft actuators namely Fiber Reinforced Elastomeric Enclosures (FREEs). FREEs are made of a hollow cylindrical tube reinforced with inextensible fibers wrapped in a helical shape on its outer surface. The tube is made of hyper-elastic materials such as latex rubber or silicone, thereby generating large strain. The angles at which the fibers are wrapped on the FREE determine its deformation behavior upon being pressurized. Depending on number of fibers and their relative angles, FREEs can generate contraction, extension, rotation, bending, or a combination of these motions. For information regarding the fabrication of FREEs, refer to [62]. As the name suggests, the BR^2 has one bending and two rotating actuators that work in tandem to achieve complex 3D spatial motions. Figure 33 shows a pressurized BR^2 and half its workspace. The work space is symmetric about the robot sagittal plane.

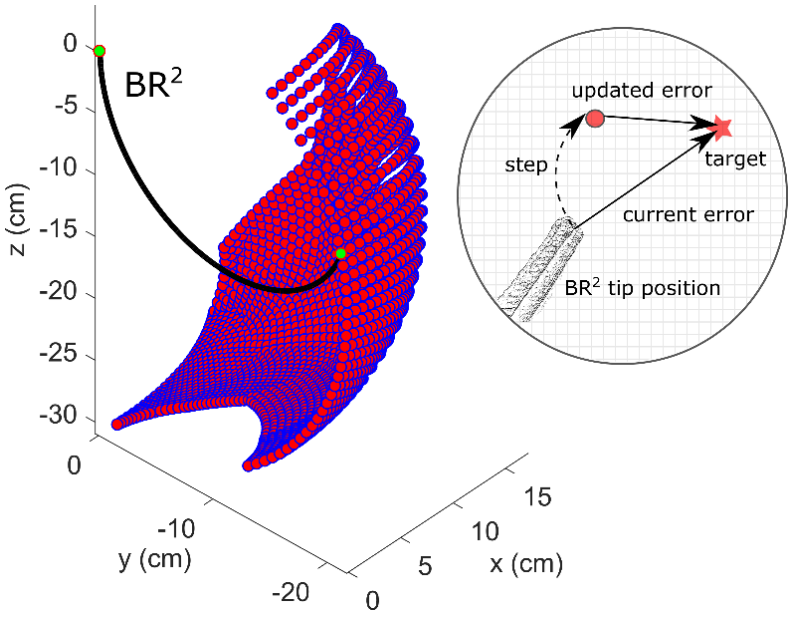

Figure 33: Half-workspace of the BR^2 manipulator. Manifold corresponds to the tip positions at different pressures. Inset: MDP formulation of the control problem.

The workspace takes the form of a convex hull that is narrower at the bottom and widens at the top with localized shearing occurring intermittently. The two modes of actuation are coupled and this manifests as a non-linear response of the BR^2 end effector position to the FREE pressure inputs at different actuation ranges. For example, the rotational sweep of the manipulator at lower bending pressures is much smaller than at higher bending pressures.

4.1 Markov Decision Process Formulation

Towards developing a robust control strategy that can account for nonlinearities inherent in soft mechanical systems the following definitions are presented. The use of reinforcement learning on a robotic system requires it to be abstracted and represented as a Markov Decision Process (MDP). An MDP is characterized by states (s), actions (a) and rewards (r). Assuming the simplest form of representation, the BR^2 manipulator is abstracted as follows:

1. State (s): States are defined as the position of continuum arm with respect to the target. The workspace around manipulator's tip is discretized into a 3D grid with a resolution of 0.01 m. The discretized grid is centered on the target location to which the tip is directed to move. Therefore, the state of the BR^2 at any given pressure is a 3D vector describing the relative distance between the manipulator tip and target location and the current actuation pressures.
2. Action (a): Each of three FREEs in the BR^2 is capable of being pressurized and depressurized. However, as the workspace is symmetric about the manipulator sagittal plane, only one half of the BR^2 workspace is considered, which corresponds to the use of the bending and one rotating FREE. Any movement in the other half of the workspace can be achieved by implementing the same actions for the second rotating FREE. The system

can produce 12 actions corresponding to different magnitudes of pressurization and depressurization. The actions for the bending FREE are: ±3.45, ±6.89, ±13.79 kPa and for the rotating FREE are ±6.89, ±13.79 and ±27.57 kPa. This enables the system to choose an optimal sequence of action to reach the target in the fewest possible steps in a robust manner.

3. Reward (r): The reward quantifies the effect an action has on the manipulator's tip position about the target. A reward system with an inductive bias is used to speed up the learning process. In our implementation, we use the L2 norm between the current tip position and target position to determine the reward and any action bringing the manipulator closer to the target returns a higher reward than an action moving it away from the target. The reward structure is described as follows:

$$r = \begin{cases} -2 + err_{prev} - err_{curr} + \zeta \\ \quad -100, P > P_{max} \\ \quad 100, \ err_{curr} \leq \varepsilon \end{cases} \tag{20}$$

The reward is structured to penalize every transition made by the system, forcing it to learn the most optimal path to the target. ζ is a tunable parameter used to penalize transitions in regions where the system becomes unstable. In this implementation, ζ corresponds to an offset from the boundaries of the workspace. By biasing the system to avoid the trajectories along the boundaries, the policy generated becomes more robust to the warping of the workspace, a common occurrence for the BR^2 arm under external loading. Furthermore, the reward structure also penalizes any action that forces the pressure in the actuators to exceed the prescribed limits. This prevents the system from getting stuck at the outer boundaries of the workspace where any additional pressurization does not change the

position of the manipulator. The system is rewarded a large positive value when a target is reached within a threshold ε.

4.2 Deep-Q Learning (DQN) Framework

Q-Learning is a model-free reinforcement learning (RL) technique that can identify an optimal action-selection policy for a given finite MDP. It is grounded on learning an action-value function which gives the expected utility for a given action when the system is at a state. A policy, Π, is a rule that the agent follows in selecting actions, given the state it is in. The value iteration update of the Q function follows the Bellman equation and is gives as:

$$Q_t(s_t, a_t) = Q_t(s_t, a_t) + \alpha(r_t + \gamma \, max_a \, Q(s_{t+1}, a) - Q_t(s_t, a_t)) \quad (21)$$

where s_t is the state of the system at time $a_t$the action it has taken to reach the new state s_{t+1}, r_t is the reward for taking action a_t, α is the learning rate, and γ is the discount factor. To account for large dimensionality, neural nets (NNs) are used to approximate the Q-functions and such frameworks are called Deep Q-Learning (DQN) networks [78]. In effect, the NN accepts states as inputs and outputs the quality associated with available actions that the system can perform and consequently, an action resulting in a larger value is considered superior. The loss function for a given state action pair is defined as the difference between the output obtained from the NN and the value obtained from the target Q-function (Q'). The optimal policy is given by the following equation.

$$\Pi(s) = max_a \, Q'(s, a) \quad (22)$$

4.3 DQN: Testing and Results

The strengths of an RL-based control system are twofold: (1) The system learns to choose an optimal sequence of actions and hence an optimal path to reach the target and (2) The system is robust to external disturbances. In this section we validate the system for its general efficacy in position control and robustness to disturbances through experiments in simulation and on a prototype of the BR^2 continuum arm. The prototype BR^2 has a length of 0.31 m with maximum operating pressures of 172.36 kPa in bending and 193.05 kPa in rotation. We use a DQN with 3 hidden layers having 512 nodes and tanh activation functions. An ε-greedy action selection strategy ($\varepsilon = 0.1$) is used while training. To expedite training, we use the model developed in [10] to train the system on a simulation. The simulation is based on a Cosserat rod formulation [5], with the elasticity and precurvature parameters fit with experimental results [79]. It is important to note that the simulation is used as a data generator for one-time data collection and the same could be done on a prototype in an automated manner. An Adam stochastic gradient optimizer (learning rate $\alpha = 0.002$) with mean-squared-error as the objective function is used to train the NN. In each episode, a tuple of points is randomly selected from the training dataset and the system is trained to transition between the two points using the ε-greedy policy. The episode is terminated in one of three ways: (1) the position error is below the threshold value, (2) number of steps exceed allowable limit and (3) the manipulator pressure exceeds the maximum rated pressure. The system is trained for 5000 episodes before evaluation. During evaluation, a greedy policy is used to select the best actions from the learned Q function to transition between states.

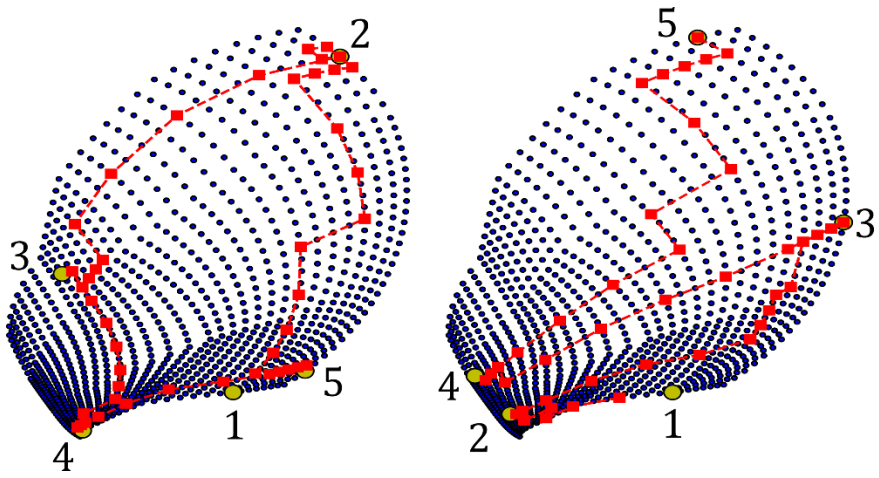

Figure 34: Path taken (shown in red) by system for two sample trajectories (1→2→3→4→5)

Figure 34 shows the path taken by the system for two sample trajectories with five waypoints each when the learned policy is evaluated. The first trajectory emphasizes on reaching extremal points that are more unlikely to be sampled during training while the second trajectory forces the system to sweep through the workspace laterally. While the position error for all the waypoints are within prescribed limits (0.01 m), two important observations can be made: (1) When transitioning between waypoints, the system takes larger strides initially and switches to smaller stride as it gets closer to the target. If the separation between the waypoints is small, the system only uses smaller strides. As seen in Figure 35, this ensures that fewer transitions are made while making sure that the target is not overshot. (2) When a target is located at the edges of the reachable workspace the system learns to avoid taking actions that would exceed the prescribed pressure limits thereby preventing it from getting stuck at a local minimum. In effect, the system learns the boundaries of the reachable workspace.

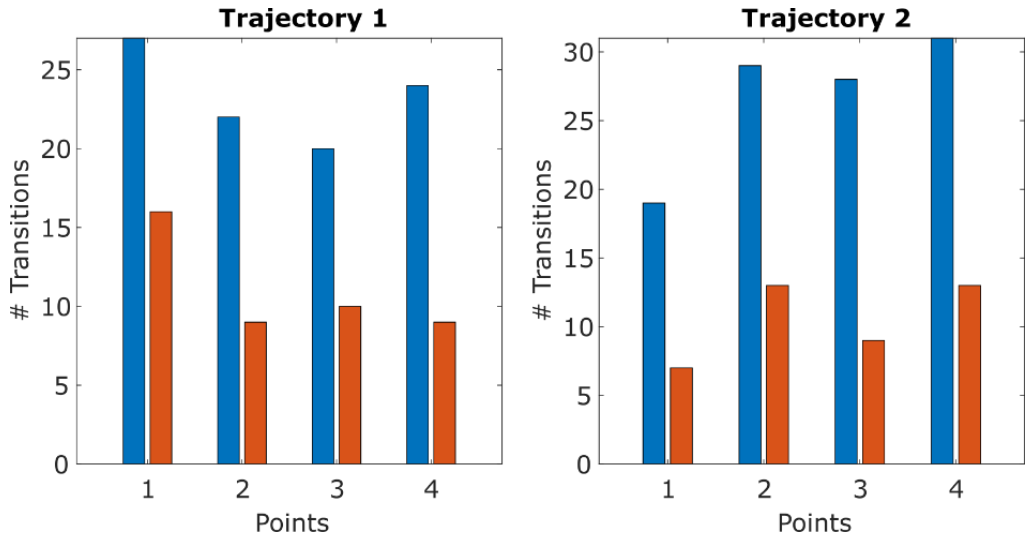

Figure 35: Effect of adaptive steps during transitions. Blue: Fixed steps and Red: Adaptive steps

Unlike conventional rigid manipulators, soft manipulators experience attenuation in their reachable workspace when loaded. Figure 36 illustrates this effect where the work space is observed to translate and distort (or shear) when a tip load is applied. To validate the robustness of the learned policy against such external loads we ran experiments with the BR^2 loaded at the tip. This draws parallels from traditional pick and place tasks in robotic manipulation. We ran experiments to evaluate the ability to generalize of the learned RL policy to different end loads. the system is trained with no external load and the learned RL policy is evaluated on different external loads. To obtain statistically significant results, 10,000 random trajectories from the reachable work spaces corresponding to the different tip loads are sampled and classified as being successful or unsuccessful. The threshold for success corresponds to a position error < 0.015 m (approximately radius of the end effector). Table 8 specifies the effect of four loads (6g, 9g, 12g, and 18g) on the accuracy of the system by detailing the number of unsuccessful attempts and the margin of error for each attempt. For reference the manipulator weighs 30g. The accuracy is observed to decrease (from 97.3% to 94.6%) with increase in tip load and this is directly correlated

to the extent by which the workspace warps. For a load of 18g the number of trajectories with an error > 0.03 m (approximately diameter of the end effector) increases rapidly and hence this region can be considered the limit above which the system may fail to perform effectively.

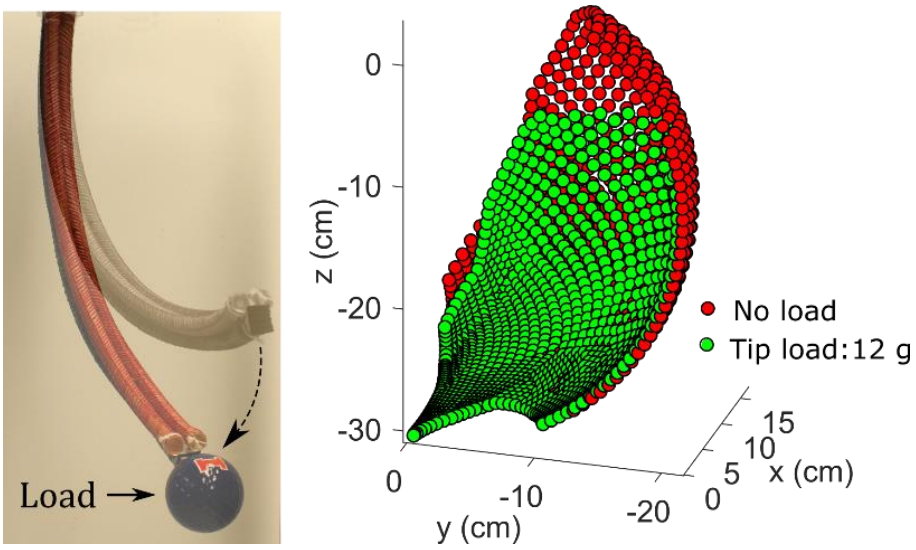

Figure 36: Effect of external loading on the effective reachable workspace of the BR^{2}manipulator

Table 8: Effect of external loads on control policy accuracy

Loads (g)	# Trajectories		
	Error ≤ 1.5 cm	1.5 cm < Error ≤ 3.0 cm	3.0 cm < Error
0	9730	249	21
6	9719	260	21
9	9588	367	45
12	9592	343	65
18	9460	376	164

To validate the results with a physical prototype of the BR^2 the setup shown in Figure 37 is used. The BR^2 is connected to a pneumatic pressure source which is controlled using a pressure regulator (SMC ITV0050-2UN). A LabVIEW interface integrated with a myRIO-1900 (National Instruments) controls the input voltage to the pressure regulator and hence the configuration of the BR^2. The tip position is captured using a 3D digitizer from MicroScribe.

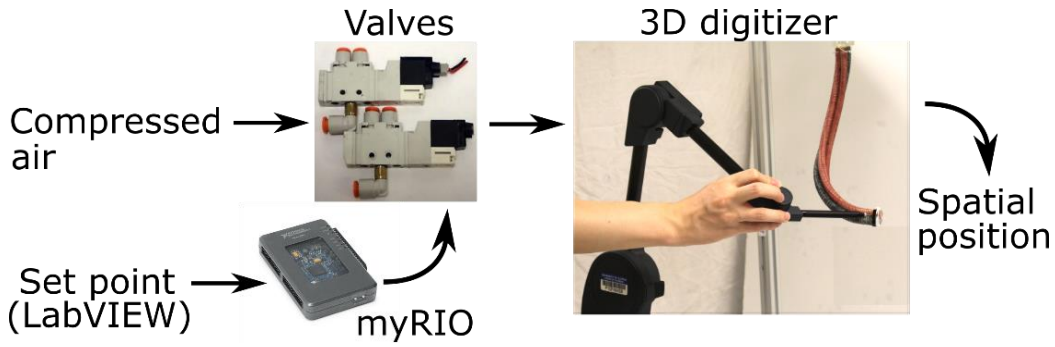

Figure 37: Validation of the system on the BR^2 prototype

A single trajectory having four waypoints is analyzed for three loading cases. The trajectory as reported in the simulation is replicated on the prototype with no feedback and therefore we expect the observed errors to be of the same order of magnitude as those reported in [80]. Two important observations highlighted in the purview of this test are: (1) The variation in input pressure required by the BR^2 to reach the same waypoints for different loads and (2) The effectiveness of the system in attempting to reach points in the unreachable workspace.

Table 9 compares the errors obtained from the simulation and experiments. The errors from the simulation indicate a robust system reaching the waypoints with a mean error of 0.48 cm (approximately 15% of the arm diameter) having a standard deviation of 0.41 cm in the reachable workspace. Results from the prototype are subject to factors like pre-curvature at zero input pressures and hysteresis during cycles of pressurization and depressurization. We report a mean error of 3.05 cm having a standard deviation of 0.97 cm for points in the reachable workspace.

This aligns with the errors reported in [80] between simulation and experimental results. To compare the error associated with points in the unreachable workspace, the corresponding nearest point in the reachable workspace for each point is used as a reference to calculate the error

*Table 9: System validation against BR^2 prototype. Unreachable points are indicated using **

Waypoint		1		2		3		4	
	Load (g)	Pressure (kPa)	Error (cm)	Pressure (kPa)	Error (cm)	Pressure (kPa)	Error (cm)	Pressure (kPa)	Error (cm)
Simulation	0	48.26,55.15	0.0	151.68,0	0.0	158.58,103.42	0.0	124.1,124.1	0.0
	6	55.15,34.47	0.37	158.58,0	0.98	158.58,75.84	1.05	131.0,103.42	0.63
	9	55.15,34.47	0.92	158.58,0	*i	162.03,62.05	*ii	134.45,96.52	0.74
	12	62.05,34.47	0.25	165.47,0	*iii	165.47,62.05	*iv	134.45,89.63	0.87
Experiment	0	48.26,55.15	3.35	151.68,0	1.20	158.58,103.42	1.62	124.1,124.1	2.98
	6	55.15,34.47	3.46	158.58,0	2.84	158.58,75.84	4.87	131.0,103.42	3.87
	9	55.15,34.47	2.72	158.58,0	*i	162.03,62.05	*i	134.45,96.52	3.68
	12	62.05,34.47	3.01	165.47,0	*iii	165.47,62.05	*iii	134.45,89.63	3.05

Table 10: Error comparison for unreachable points in experiments with BR^2 prototype

Points	i	ii	iii	iv
Distance to closest point in reachable workspace (cm)	1.65	1.31	2.18	1.65
Distance to BR^2 tip position from simulation (cm)	1.65	1.60	2.48	1.79
Distance to BR^2 tip position from prototype (cm)	2.10	4.29	0.90	3.05

. The results are tabulated in Table 9. For simplicity the unreachable points are labeled (i-iv) from Table 10. The points are tracked robustly in simulation with the maximum variation in error of 0.31 cm (approximately 10% of the arm diameter). In case of the prototype, the maximum variation is 2.98 cm (approximately the arm diameter).

4.4 Deep Deterministic Policy Gradient (DDPG)

As highlighted in the previous sections, the BR^2 traces a highly nonlinear workspace with variable stiffness characteristics as a function of pressure input and tip orientation. To improve manipulability, the BR^2 is mounted on a swiveling base making it a more dexterous and redundant system. Furthermore, the swiveling BR^2 operates in a discontinuous workspace, where a direct path connecting two arbitrary points in the workspace is not always feasible. The accumulated effects of nonlinearity, redundancy and discontinuity makes the swiveling BR^2 a complex system to control with existing model-based methods. Towards establishing an effective control scheme, we propose using a model-free approach for tip position control. It is important to note that for the control scheme explored in this work, the forward model is used as proxy for the physical prototype to enable rapid collection of data. As the controller being designed is not derived analytically from the forward model our approach is model-free. We outline the following requirements from the proposed control scheme:

1. Effectively perform multi-point tracking
2. Exhibit load invariant policies within bounds. Bounds are determined by degree of workspace attenuation.
3. Control policy should be stable for points in the unreachable workspace and discontinuous regions of the workspace.
4. Control policy should be effectively deployed in a physical prototype.

In this work, a model-free reinforcement learning (RL) technique suited for continuous actions is adopted. Assuming the simplest form of representation, the swiveling BR^2 manipulator is abstracted as follows:

1. State (s): The state, $s \in R^6$ encodes the error of the tip position and the actuation inputs. $s = [\delta x, \delta y, \delta z, P_b, P_r, P_\theta]$, where the first three components describe the position error with respect to a target and the last three components are the bending, rotating and swiveling inputs.
2. Action (a): Each component of the swiveling BR^2 is capable of continuous actions, the bounds on which are, ±31.2 kPa in bending, ±96.5 kPa in rotating and ± 60^o in swiveling.
3. Reward (r): The reward quantifies the effect an action has on the manipulator's tip position about the target. A reward system with an inductive bias is used to speed up the learning process. The reward structure is described as follows:

$$r = \begin{cases} -2 + err_{prev} - err_{curr} \\ -2 + err_{curr}, P > P_{max} \;||\; iter > iter_{max} \\ 100,\ err_{curr} \leq \varepsilon \end{cases} \tag{23}$$

The reward is structured to penalize every transition made by the system, forcing it to learn the most optimal path to the target. The system is rewarded a large positive value when a target has been reached within a threshold (ε = 1.5 cm).

DDPG is a well-established model-free RL approach suited for continuous control applications. Our implementation of DDPG uses an actor-critic formulation to enable generation of complex and robust policies. The "actor" network accepts the current state of the BR^2 as input and generates a continuous action as the output while the "critic" network evaluates the quality of the state-actor tuple. The aim of the RL framework is to maximize the Q-values obtained from the critic network as a function of the weights of the actor network. We adopt a framework using experience replay

and soft updates to ensure robustness and stability during the learning process [60]. The critic network is updated using Equation 21 and the actor uses gradients obtained from the "Deterministic Policy Gradient" theorem [81]. The gradient from Equation 24 is used to train actor network using a stochastic gradient ascent approach.

$$\nabla_\theta Q = \boldsymbol{E}\left[\nabla_\theta \mu(s|\theta)\, \nabla_a Q(s, a = \mu(s)|w)\right] \quad (24)$$

where w and θ are the weights of the critic and actor networks, μ is the actor policy and a is the action output from the actor network. The efficacy of RL-based control strategies depends on the ability of the robotic agent to explore the state-action space effectively during training. Exploration is carried out by incorporating noise into the control actions dictated by the actor network. We use an "Orienstein-Uhlenbeck" process (Equation 25) to generate noise. The magnitude of the noise is directly proportional to the size of the step taken by the agent. Consequently, larger action would incur greater noise thereby increasing the chances of the agent becoming unstable (exceeding max input levels or overshooting the target). Therefore, while the reward formulation promotes taking larger actions, the exploration noise favors taking smaller actions. The authors believe that the combined effects of these two factors enables the agent to take moderate steps that converge to the target effectively.

$$\delta a = \varphi(\zeta - a) + \sigma N(0,1) \quad (25)$$

4.5 DDPG: Testing and Results

The DDPG framework is trained using an actor and critic network each having two hidden layers with 500 neurons each. The outputs for the actor are bounded between -1 and +1 using $tanh$ activation functions. An Adam optimizer is used to train the network using backpropagation with a learning rate of 2e-5 for the actor and 1e-4 for the critic network. The soft update parameter is set to 1e-2 and the framework is trained for 50000 episodes. The framework is validated on three

curves: (i) Horizontal line, (ii) Circle and (iii) Viviani's Curve. Figure 38 illustrates the curves and the configurations of the manipulator during path tracking. Figure 38 also details the variation in the input to the BR^2 as a function of waypoints. The oscillations in the inputs are indicative of the complexity of the curve being tracked. Lastly, the tip position error is bounded to $\leq$ 3.0 cm (approximately tip diameter of the BR^2). A more rigorous error analysis is detailed in the following paragraph.

Effect of Loading: As mentioned previously, tip loading can have significant impact on the reachable workspace of the BR^2 manipulator. Therefore, it becomes important to validate any control strategy's effectiveness in the presence of external loads. Towards establishing an upper bound on the load that our control strategy can adapt to, the following study is conducted. The manipulator is loaded at the tip with a point load and the path tracking task executed. The BR^2 weighs $\approx$ 30g and we choose three loads (3g, 6g and 9g) corresponding to 10%, 20% and 30% of the body weight to assess the efficacy of the control policy. The loads are also chosen to maximize the reachability of the waypoints of the test curves being tracked for the prescribed actuation limits. It can be observed that the error for varying loads remains bounded and displays similar trends that are characterized by valleys and peaks as shown in Figure 39. The peak errors correspond to points that fall outside the reachable workspace. Table 11 details the error statistics for the study. Note: Certain configurations (shown in red) in the loaded conditions could not be solved as the boundary value formulation was unable to converge to a feasible solution. However, as seen later, the control framework can compensate for such irregularities and perform effectively even for such configurations.

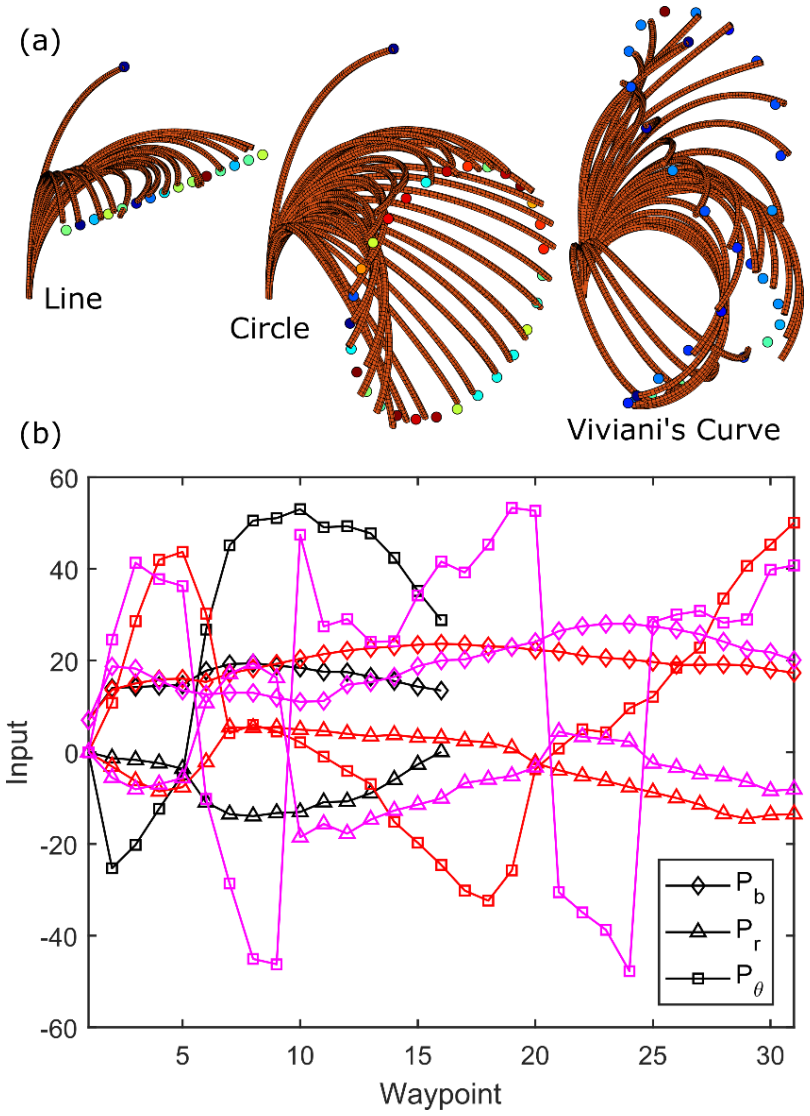

Figure 38: (a) Validation curves for assessing the performance of control policy. (b) Variation in inputs for line (black), circle (red) and Viviani's curve(magenta). The swiveling BR^2 modulates three inputs to reduce position error for each waypoint. Oscillations in the inputs are indicative of the complexity of the task for the manipulator. All curves lie in the reachable workspace. The following error statistics are reported for each curve: 0.83±0.30cm for horizontal line, 0.71±0.21cm for circle and 0.93±0.57cm for Viviani's curve.

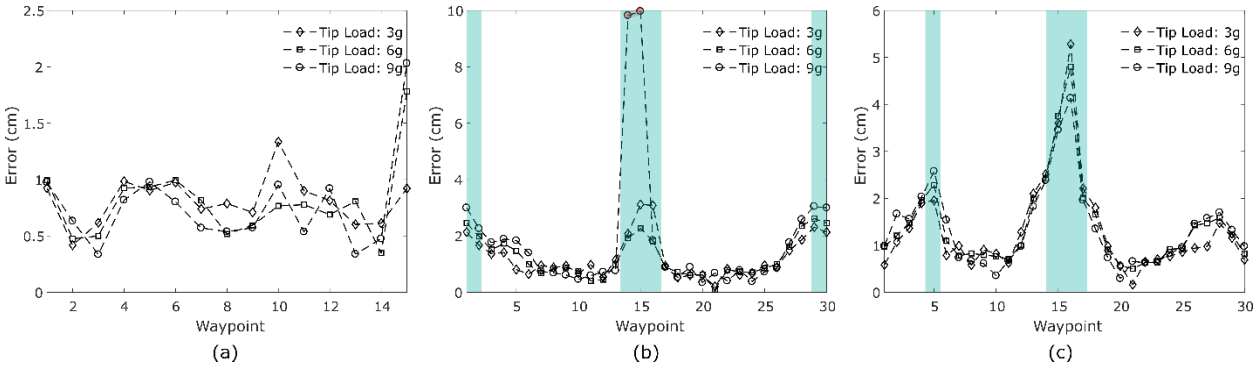

Figure 39: Variation in tip position error for the three test curves for different tip loads. The trend indicates an adaptable policy that can account for loads as high as 9g. Trends in the error variations are accompanied by peaks (highlighted) which correspond to points that lie outside the reachable workspace. Points shown in red correspond to configurations that did not converge to a solution. At higher loads (> 9g) the manipulator is not able to effectively navigate the workspace for the prescribed actuator input limits.

Table 11: Error statistics for effect of external loads. Error is reported in cm.

Curves	3g	6g	9g
Line	0.82±0.22	0.79±0.34	0.76±0.42
Circle	0.82±0.22	1.23±0.72	1.84±2.34
Viviani's Curve	1.34±1.04	1.40±0.95	1.37±0.89

Effect of Reachability: In this study we analyze the systems capability to handle points in the unreachable workspace. While a simple inverse kinematics formulation would potentially return infeasible solutions in such cases, an RL-based system is able to overcome these limitations. 200 random target points are sampled from the reachable workspace and perturbed such that they become unreachable. The points are perturbed along the vector connecting the point to the origin.

The maximum perturbation corresponds to a magnitude of 8 cm. The performance of the system is measured as a difference between the closest the BR^2 gets to the target and the closest point in the reachable workspace. Figure 40 details the results from this study. In most instances, (76%) the system can obtain errors smaller than the induced perturbation by finding better manipulator configurations. In certain configuration the error remains larger and this has been found to occur in extreme configurations.

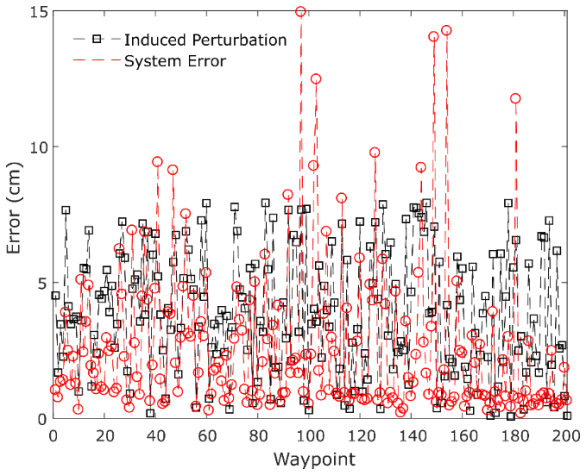

Figure 40: Variation in position error due to induced perturbation. The average perturbation is 3.9±2.3 cm and the average reported system error is 2.6±2.7 cm.

Effect of Workspace Discontinuity: In this study, when training in simulation we intentionally create a discontinuity in the BR^2 workspace by limiting the swiveling base rotation to $\pm 60^0$ as shown in Figure 41. The discontinuity makes navigating the workspace challenging. Traversing to a target point would necessitate taking large steps using more complex policies and the use of spatially localized exploration techniques and trajectory optimization for path tracking may prove ineffective in such scenarios [82]. In Figure 41, three trials consisting of two points that lie on either side of the discontinuity are chosen and the BR^2 is instructed to move between them. With

the inclusion of input pressures in the state and extensive bootstrapping of the workspace during training the DDPG framework learns to navigate around the discontinuity towards the target.

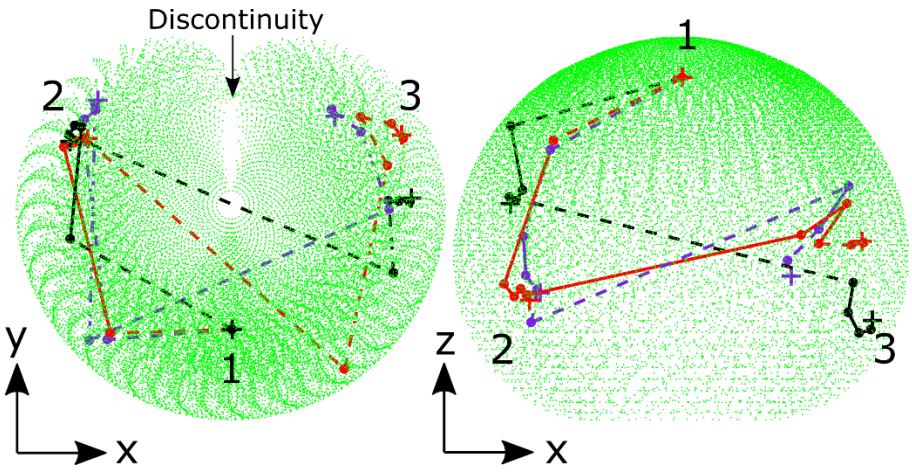

Figure 41: Three paths taken by the BR^2 when moving from points in regions 1→2→3. The points are separated by a discontinuity that the manipulator cannot navigate across. The paths taken demonstrate the DDPG's capability to account for discontinuities in a manipulator's workspace. '+' target waypoints, '·' intermediate waypoints chosen by the system.

4.6 Experimental Results and Bias Mitigation Using Feedback

We hypothesize that a learned control policy, tuned in simulation for path tracking, can perform to the same degree of accuracy in a physical prototype (as in simulation) by incorporating state feedback. Towards studying the effect of feedback, path tracking experiments were conducted and compared in both open loop and closed loop settings. As seen in Figure 42, eight VICON T40 motion capture cameras are used to capture the tip position of the BR^2. Transferring a control policy from a simulation to prototype will result in position errors due to biases from two sources: (1) Static inaccuracies, that arises from factors including precurvature of the actuators, hysteresis and varying control resolution between simulation and prototype and (2) Kinematic inaccuracies during path tracking due to non-commutative nature of the actuation. The non-commutativity

makes transitioning between two pressure states P_1 and P_2 path dependent, where the final position of the BR^2 at P_2 depends on P_1 due to varying initial stiffness. The combined error from these sources manifests as large position errors which is reported in Figure 43 when an open loop scheme is implemented. To overcome these effects, the manipulator is incorporated into a feedback system and the bias mitigation can be observed in Figure 43 and Table 12. Figure 43 (d) illustrates the trend in the number of transitions as reported during the studies. We observe convergence to minimum error more quickly in simulations compared to experiments. For experiments, the loaded configurations take more iterations when compared to configurations with no load. This can be attributed to the system compensating for additional tip deformations (due to tip load) that could not be accounted for during training. Finally, the number of iterations also increases with the complexity of the curve being tracked.

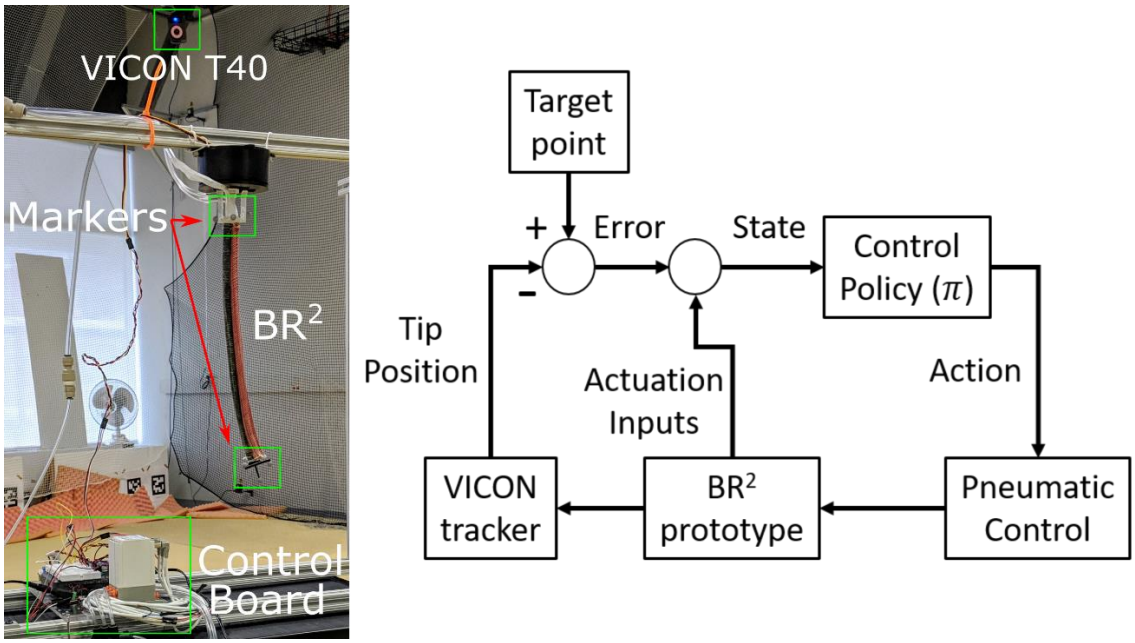

Figure 42: Experimental setup for feedback control deployed on the BR^2 manipulator. BR^2 tip position is tracked using a VICON motion capture system using eight VICON T40 cameras.

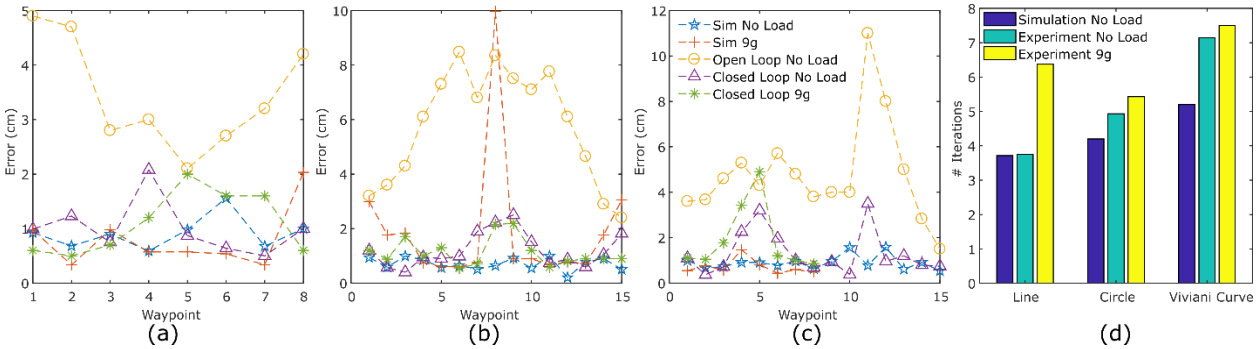

Figure 43: Effect of feedback on tracking error for (a) Line, (b) Circle and (c) Viviani's curve for unloaded and loaded conditions. The feedback errors are observed to be bounded for all points within the reachable workspace while points outside the reachable workspace have larger errors. (d) Variation in the average number of iterations for different curves in simulation and experiments. Note: The maximum number of iterations is set to 15 for each waypoint.

Table 12: Error statistics for effect of external loads. Error is reported in cm.

Curves	Open loop (No load)	Closed loop (No load)	Closed loop (9g)
Line	3.45±1.02	1.01±0.49	1.10±0.58
Circle	5.77±2.08	1.21±0.61	1.13±0.51
Viviani's Curve	4.81±2.23	1.32±0.97	1.91±1.47

CHAPTER 5: CONCLUSION

Purpose: The thesis deals with two important facets in the research of soft mechanical systems, namely design and controls. Soft systems deform as a continuum and cannot be mechanically modeled as a system with finite degrees of freedom. The resulting conundrum has created a gap, where traditional design and control techniques are deemed unsuitable for soft systems. This thesis aims to bridge the gap, allowing the use of conventional design methods that have resulted from over a century's worth of research in kinematics in designing novel embodiments of soft mechanisms. The bridge is enabled by reduced order models that can capture the deformation behavior of a specialized, yet ubiquitous soft actuator building block known as fiber reinforced elastomeric enclosures (FREEs). Likewise, in the realm of controls, classical model-based controls are less suitable for soft systems as it requires the estimation of all the states associated with the large number of degrees of freedom. This thesis, for the first time demonstrates the efficacy of model-free Reinforcement Learning (RL) methods for the control of a unique soft manipulator.

Importance: The importance of this thesis is that soft system designers have an arsenal of reduced order models and design techniques to systematically generate feasible solutions. Furthermore, the thesis provides control engineers with a possible framework to implement model-free learning-based control techniques of soft robots that can be robust to external disturbances.

Impact: The thesis primarily impacts the design and deployment of soft robots. The soft mechanical systems considered in this thesis are the structural embodiments of soft robots. This is especially relevant in soft biologically inspired robots where the performance of muscle-like actuators cannot be tailored for a given requirement using rigid transmission components (such as gears or belts and pulleys). In such a scenario, the thesis proposes a spatial topology of actuators

that can be designed to tune the stroke and force from the system. Specifically, the obtained designs are impactful in soft wearable active exoskeletons that could enhance the upper-limb mobility of healthy and disabled humans. The control techniques presented in the thesis are specifically relevant for soft continuum manipulators for use in agricultural applications such as berry harvesting, imaging and weeding, with additional impact in manufacturing and human-computer interaction.

5.1 Contribution

The thesis makes distinct contributions to the model-based design and model-free control of soft mechanical systems.

5.1.1 Contribution in Design

Traditionally, analysis of soft self-actuating mechanisms is challenging because of the nonlinearity due to large deformations and hyper-elastic material properties. These result in a set of coupled partial differential equations that are typically solved using computationally expensive Finite Element packages. Furthermore, there is a dearth of a systematic synthesis framework for soft mechanical systems. The thesis makes an attempt to address these issues in the design of soft robotics through the following contributions.

1. The thesis aims to formulate a lumped Pseudo-Rigid Body (PRB) model to analyze a specific soft building block known as Fiber Reinforced Elastomeric Enclosures (FREEs). We lay out an elaborate framework to fit the model parameters such that the transverse deflection can be captured with less than 10-15% accuracy. Using the PRB model, a mechanism composed of a planar combination of FREEs can be analyzed quickly, as they reduce to finding roots for a set of nonlinear polynomial equations. Perhaps the most

important advantage of the PRB model is the ability to quickly evaluate design concepts and incorporate it within an optimization framework.

2. The thesis proposes a second reduced order model termed as the Homogenized Strain Induced Model (HSIM) that can capture the force-stroke deformation characteristics of FREEPAMs at varying pressures is analyzed. The model is data driven and its validity is verified in simulation and an error analysis reports a maximum error of 4.4% when compared to high fidelity FEA simulations.
3. The thesis investigates a prospective design method for soft mechanisms by systematically combining a fundamental building block known as pennate building block (PBB). Similar to human muscles the PBB was found to amplify stroke of actuation based on configuring the pennate angle between the contracting actuators. Several mechanisms were obtained by systematically combining PBBs including a planar gripper, motor, spatial compression sleeve, cylindrical contracting member. These mechanisms were analyzed for their deformation and forces using HSIM, PRBM and prototyped to validate accuracy.
4. Lastly, the thesis investigates a systematic design methodology of compliant systems with a combination of active and passive members. The design framework begins with conceptual topology synthesis based on load-flow visualization and culminates with optimization-based design refinement. A planar shape-morphing airfoil example was designed using this method.

5.1.2 Contribution in Controls

The second focus of this thesis showcases the use of deep reinforcement learning (RL) as a viable approach for generalized position control for a novel pneumatic continuum arm known as the BR2

that deforms by combining spatial bending and torsion. The contributions can be summarized as follows:

1. Through a valid training and testing scheme, the efficacy of RL based approach has been attested to for two RL frameworks: Deep Q-Learning and Deep Deterministic Policy Gradients.
2. Both systems exhibit two important features, which are (a) its ability to choose appropriate actions to reduce the number of transitions and (b) its considerable robustness to external loads including self-weight. The system is also validated for its ability to reach the best possible configuration in cases where the target lies in the unreachable work space. The results clearly indicate that reinforcement learning can emerge as a viable technique for learning control policies for complex continuum manipulators which are otherwise hard to model and control using methods based on first principles alone.
3. The thesis also explores incorporating the system with sensors to create a framework with real time feedback of the BR^2's tip position. Closed loop control, coupled with online policy adaptation based on state feedback, significantly improves the overall training time of such soft systems.

5.2 Future Work

While this thesis has fundamental contributions in the design and control of soft mechanical systems, it sets the stage for future developments in the field which can be highlighted as follows: (1) The reduced order models for design were investigated for static quasistatic conditions alone. While this gives preliminary insight, there is a need to extend the models to incorporate dynamics. The lumped PRB and the continuum HSI models proposed in this thesis will then have additional

parameters that capture inertia of the manipulator. This warrants more experiments to characterize and validate the model.

(2) The reinforcement learning framework for controls was also formulated for quasistatic conditions. However, most manipulators have a very different, and often larger dynamic workspace, which can be exploited to good use in practical applications. Extension of the RL scheme to incorporate dynamics is envisaged as future work. Additionally, this work potentially establishes a baseline for exploring other RL paradigms that offer alternate modes of control like stiffness/ force control and obstacle avoidance. It can also provide a good case study for emerging work in simulation-to-real learning and transfer learning paradigms, such as Target Apprentice based Transfer Learning or Meta Learning.

(3) The thesis showcased and tested several designs that constitute periodic arrangement of actuator dyads to tailor the stroke and force output. However, the design methodology must be extended to creating aperiodic combinations of actuators that can yield more complex deformation profiles. A preliminary example was illustrated in the form of shape morphing wheel shown in Figure 22 , but no systematic design methodology for these requirements were proposed. Future work entails a design methodology for active metamaterials periodic/aperiodic building blocks that yield a given performance requirement.

APPENDIX: DATA COLLECTION

This section details the experiments conducted to determine the bending behavior of FREEs, which in turn is used to validate the FE model used for data collection. Three categories FREEs with different fiber angles α= (25^{o},30 ^{o},40 ^{o}) were fabricated. Under each category, three FREEs with lengths l= (78, 110.5, 130) mm, radius r= 13 mm, and denoted by slenderness ratio (ratio of FREE length to diameter) λ= (6,8.5,10) were fabricated and subject to three actuation pressures, P_a= (15,17.5,20) psi, along with transverse bending loads. The experimental setup is shown in Figure 44: Bending test setup. FREEs are constrained at one end and the other end is subjected to a planar transverse end load and the FREE's tip deflection is recorded. Excessive loading is avoided to ensure that no part of the FREE undergoes buckling or kinking. To account for hysteresis each data point is recorded as the mean of multiple trials. This study is used to validate the FEM model, which can then be used as a suitable surrogate for experimental data collection with reasonable confidence. The axial parameters of the FREE such as the actuation force f_a on the linear springs have already been verified by the authors' previous publications [83] and other researchers [66] [63].

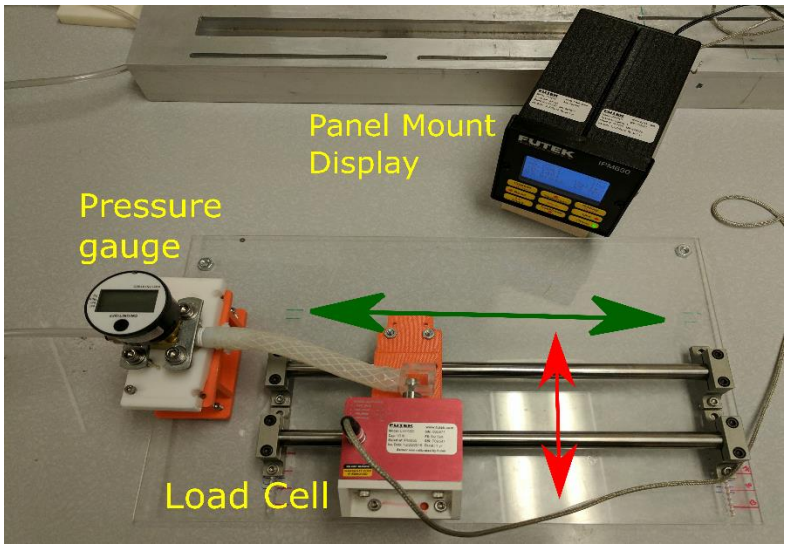

Figure 44: Bending test setup

Results of the comparison between experiments and FEA for λ = (6,8.5,10) are tabulated in Table 13. Each observation corresponds to the mean error between experimental and simulated tip position for three transverse loads, divided by the tip displacement obtained from experiments. The relatively large errors can be explained as follows. When FREEs are subjected to small loads the tip deflections are also relatively small. In such cases, even a small deviation (~2 mm) compounded by the resolution of readings from experiments (±2 mm) can reflect as large errors. An example in this regard would be the FREE, λ =6, α=25^o, P_a=15 psi subjected to a transverse load of 0.098 N. We observe (x_{exp}, y_{exp}) = (16,1) and (x_{fem} , y_{fem})=(13.1,2.16) which translates to an error of 19.48 % . Another important observation is the reduction in error with increase in λ. This occurs because for the same transverse load, the tip deflection increases with λ, thereby reducing the percent error.

Table 13: FEM Model Error (%)

λ	P_a	$\alpha = 25^o$	$\alpha = 30^o$	$\alpha = 40^o$
6	20	15.12	17.88	17.23
	17.5	13.14	17.26	17.96
	15.0	17.7	17.38	12.84
8.5	20	8.52	7.95	9.91
	17.5	10.77	11.03	8.33
	15.0	13.45	9.03	6.77
10	20	2.45	8.01	7.84
	17.5	5.88	6.21	4.75
	15.0	6.86	10.20	6.92

REFERENCES

[1] G. Krishnan, J. Bishop-Moser, C. Kim, and S. Kota, "Evaluating mobility behavior of fluid filled fiber-reinforced elastomeric enclosures," in *ASME 2012 International Design Engineering Technical Conferences and Computers and Information in Engineering Conference*, 2012, pp. 1089–1099.

[2] G. Krishnan, J. Bishop-Moser, C. Kim, and S. Kota, "Kinematics of a Generalized Class of Pneumatic Artificial Muscles," *ASME J. Mech. Robot.*, vol. 51, p. 61801, 2015.

[3] Y. Shan, M. P. Philen, C. E. Bakis, K. W. Wang, and C. D. Rahn, "Nonlinear-elastic finite axisymmetric deformation of flexible matrix composite membranes under internal pressure and axial force," *Compos. Sci. Technol.*, vol. 66, no. 15, pp. 3053–3063, 2006.

[4] G. Singh and G. Krishnan, "An Isoperimetric Formulation to predict Deformation Behavior of Pneumatic Fiber Reinforced Elastomeric Actuators," in *IEEE International Conference on Intelligent Robots and Systems*, 2015, pp. 1738–1743.

[5] D. Trivedi, A. Lotfi, and C. D. Rahn, "Geometrically exact models for soft robotic manipulators," *IEEE Trans. Robot.*, vol. 24, no. 4, pp. 773–780, 2008.

[6] D. Trivedi, "Modeling, Optimal Design, Shape Estimation and Workspace," The Pennsylvania State University, 2010.

[7] S. S. Antman, "Nonlinear Problems of Elasticity, 1995." Springer.

[8] I. D. Walker, R. Mattfeld, A. Mutlu, A. Bartow, and N. Giri, "A novel approach to robotic climbing using continuum appendages in in-situ exploration," in *2012 IEEE Aerospace Conference*, 2012, pp. 1–9.

[9] N. K. Uppalapati, G. Singh, and G. Krishnan, "Parameter estimation and modeling of a pneumatic continuum manipulator with asymmetric building blocks," in *2018 IEEE*

International Conference on Soft Robotics (RoboSoft), 2018, pp. 528–533.

[10] N. K. Uppalapati and G. Krishnan, “Towards Pneumatic Spiral Grippers: Modeling and Design Considerations,” *Soft Robot.*, vol. 5, no. 6, pp. 695–709, Dec. 2018.

[11] T. G. Thuruthel, E. Falotico, F. Renda, and C. Laschi, “Model-Based Reinforcement Learning for Closed-Loop Dynamic Control of Soft Robotic Manipulators,” *IEEE Trans. Robot.*, pp. 1–11, 2018.

[12] A. Melingui, R. Merzouki, J. B. Mbede, C. Escande, B. Daachi, and N. Benoudjit, “Qualitative approach for inverse kinematic modeling of a compact bionic handling assistant trunk,” in *Neural Networks (IJCNN), 2014 International Joint Conference on*, 2014, pp. 754–761.

[13] M. Giorelli, F. Renda, G. Ferri, and C. Laschi, “A feed-forward neural network learning the inverse kinetics of a soft cable-driven manipulator moving in three-dimensional space,” in *2013 IEEE/RSJ International Conference on Intelligent Robots and Systems*, 2013, pp. 5033–5039.

[14] T. Zheng, I. S. Godage, D. T. Branson, R. Kang, E. Guglielmino, and D. G. Caldwell, “Octopus Inspired Walking Robot: Design, Control and Experimental Validation,” *IEEE Int. Conf. Robot. Autom.*, pp. 816–821, 2013.

[15] Ying Shan *et al.*, “Variable Stiffness Structures Utilizing Fluidic Flexible Matrix Composites,” *J. Intell. Mater. Syst. Struct.*, vol. 20, no. 4, pp. 443–456, 2009.

[16] L. Peel, “Fabrication and Mechanics of Fiber-Reinforced Elastomers,” Brigham Young University, Provo, UT, USA, 1998.

[17] G. K. Klute, J. M. Czerniecki, and B. Hannaford, “McKibben artificial muscles: pneumatic actuators with biomechanical intelligence,” in *Advanced Intelligent*

Mechatronics, 1999. Proceedings. 1999 IEEE/ASME International Conference on, 1999, pp. 221–226.

[18] G. Singh and G. Krishnan, "An isoperimetric formulation to predict deformation behavior of pneumatic fiber reinforced elastomeric actuators," in *2015 IEEE/RSJ International Conference on Intelligent Robots and Systems (IROS)*, 2015, pp. 1738–1743.

[19] F. Connolly, P. Polygerinos, C. J. Walsh, and K. Bertoldi, "Mechanical programming of soft actuators by varying fiber angle," *Soft Robot.*, vol. 2, no. 1, pp. 26–32, 2015.

[20] D. Trivedi, A. Lotfi, and C. D. Rahn, "Robotic Manipulators," vol. 24, no. 4, pp. 773–780, 2008.

[21] D. Trivedi, "Modeling, Optimal Design, Shape Estimation and Workspace," The Pennsylvania State University, 2010.

[22] N. Giri and I. D. Walker, "Three module lumped element model of a continuum arm section," *2011 IEEE/RSJ Int. Conf. Intell. Robot. Syst.*, pp. 4060–4065, Sep. 2011.

[23] I. D. Walker, R. Mattfeld, A. Mutlu, A. Bartow, and N. Giri, "A novel approach to robotic climbing using continuum appendages in in-situ exploration," in *2012 IEEE Aerospace Conference*, 2012, pp. 1–9.

[24] D. Trivedi, D. Dienno, and C. D. Rahn, "Optimal, Model-Based Design of Soft Robotic Manipulators," *J. Mech. Des.*, vol. 130, no. 9, p. 091402, 2008.

[25] A. Midha and L. L. Howell, "A method for the design of compliant mechanisms with small-length flexural pivots," *ASME J. Mech. Des*, vol. 116, pp. 280–290, 1994.

[26] A. Midha and L. L. Howell, "Evaluation of equivalent spring stiffness for use in a pseudo-rigid-body model of large-deflection compliant mechanisms," *J. Mech. Des.*, vol. 118, p. 127, 1996.

[27] A. MIdha, “Parametric deflection approximations for end-loaded, large-deflection beams in compliant mechanisms,” *J. Mech. Des.*, vol. 117, p. 157, 1995.

[28] D. Trivedi, C. D. Rahn, W. M. Kier, and I. D. Walker, “Soft robotics: Biological inspiration, state of the art, and future research,” *Appl. Bionics Biomech.*, vol. 5, no. 3, pp. 99–117, 2008.

[29] D. C. Rucker, B. A. Jones, and R. J. Webster III, “A geometrically exact model for externally loaded concentric-tube continuum robots,” *IEEE Trans. Robot.*, vol. 26, no. 5, pp. 769–780, 2010.

[30] S. Grazioso, G. Di Gironimo, and B. Siciliano, “A Geometrically Exact Model for Soft Continuum Robots: The Finite Element Deformation Space Formulation,” *Soft Robot.*, p. soro.2018.0047, Nov. 2018.

[31] N. K. Uppalapati and G. Krishnan, “Towards Pneumatic Spiral Grippers: Modeling and Design Considerations,” *Soft Robot.*, p. soro.2017.0144, Jul. 2018.

[32] S. Satheeshbabu and G. Krishnan, “Designing systems of fiber reinforced pneumatic actuators using a pseudo-rigid body model,” in *2017 IEEE/RSJ International Conference on Intelligent Robots and Systems (IROS)*, 2017, pp. 1201–1206.

[33] C. Majidi, R. F. Shepherd, R. K. Kramer, G. M. Whitesides, and R. J. Wood, “Influence of surface traction on soft robot undulation,” *Int. J. Rob. Res.*, vol. 32, no. 13, pp. 1577–1584, Nov. 2013.

[34] H. Habibi, R. Kang, I. D. Walker, I. S. Godage, and D. T. Branson, “Developing a 3-D, Lumped-Mass Model to Present Behaviour of Large Deformation Surface Based Continuum Robots,” in *IUTAM Symposium on Intelligent Multibody Systems–Dynamics, Control, Simulation*, 2019, pp. 133–147.

[35] Y. Hao *et al.*, “A eutectic-alloy-infused soft actuator with sensing, tunable degrees of freedom, and stiffness properties,” *J. Micromechanics Microengineering*, vol. 28, no. 2, p. 024004, Feb. 2018.

[36] M. Ashby, “Designing architectured materials,” *Scr. Mater.*, vol. 68, no. 1, pp. 4–7, 2013.

[37] S. K. Patiballa and G. Krishnan, “Qualitative Analysis and Conceptual Design of Planar Metamaterials With Negative Poisson’s Ratio,” *J. Mech. Robot.*, vol. 10, no. 2, p. 021006, Feb. 2018.

[38] Q. Wang, J. A. Jackson, Q. Ge, J. B. Hopkins, C. M. Spadaccini, and N. X. Fang, “Lightweight Mechanical Metamaterials with Tunable Negative Thermal Expansion,” *Phys. Rev. Lett.*, vol. 117, no. 17, p. 175901, Oct. 2016.

[39] C. M. Eng, E. Azizi, and T. J. Roberts, “Structural determinants of muscle gearing during dynamic contractions,” *Integr. Comp. Biol.*, 2018.

[40] D. Lee, Z. Li, Q. Z. Sohail, K. Jackson, E. Fiume, and A. Agur, “A three-dimensional approach to pennation angle estimation for human skeletal muscle,” *Comput. Methods Biomech. Biomed. Engin.*, vol. 18, no. 13, pp. 1474–1484, 2015.

[41] A. I. Nawroj and A. M. Dollar, “Shape Control of Compliant, Articulated Meshes: Towards Modular Active-Cell Robots (MACROs),” *IEEE Robot. Autom. Lett.*, vol. 2, no. 4, pp. 1878–1884, 2017.

[42] A. I. Nawroj and A. M. Dollar, “Evaluation of regular planar meshes for Modular Active Cell Robots (MACROs),” in *Intelligent Robots and Systems (IROS), 2017 IEEE/RSJ International Conference on*, 2017, pp. 6434–6439.

[43] P. Polunin *et al.*, “Characterizing MEMS nonlinearities directly: The ring-down measurements,” in *Solid-State Sensors, Actuators and Microsystems (TRANSDUCERS),*

2015 Transducers-2015 18th International Conference on, 2015, pp. 2176–2179.

[44] B. Trease and S. Kota, "Design of Adaptive and Controllable Compliant Systems With Embedded Actuators and Sensors," *J. Mech. Des.*, vol. 131, no. 11, p. 111001, Nov. 2009.

[45] A. P. Milojević and N. D. Pavlović, "Development of a new adaptive shape morphing compliant structure with embedded actuators," *J. Intell. Mater. Syst. Struct.*, vol. 27, no. 10, pp. 1306–1328, Jun. 2016.

[46] A. Milojević, N. D. Pavlović, S. Linß, M. Tomić, N. T. Pavlović, and H. Handroos, "A Concept of Adaptive Two Finger Gripper with Embedded Actuators," in *Microactuators and Micromechanisms*, Springer, 2017, pp. 239–250.

[47] A. Milojevic, S. Linβ, Z. Cojbasic, H. Handroos, L. Luostarinen, and L. Zentner, "Adaptive Soft Robotic Gripper Based on Shape Morphing Compliant System," in *2018 International Conference on Reconfigurable Mechanisms and Robots (ReMAR)*, 2018, pp. 1–10.

[48] M. Shibata, F. Saijyo, and S. Hirai, "Crawling by body deformation of tensegrity structure robots," in *Robotics and Automation, 2009. ICRA'09. IEEE International Conference on*, 2009, pp. 4375–4380.

[49] K. Caluwaerts *et al.*, "Design and control of compliant tensegrity robots through simulation and hardware validation," *J. R. Soc. interface*, vol. 11, no. 98, p. 20140520, 2014.

[50] M. S. Malekzadeh, S. Calinon, D. Bruno, and D. G. Caldwell, "Learning by imitation with the STIFF-FLOP surgical robot: a biomimetic approach inspired by octopus movements," *Robot. Biomimetics*, vol. 1, no. 1, p. 13, Dec. 2014.

[51] C. Laschi, M. Cianchetti, B. Mazzolai, L. Margheri, M. Follador, and P. Dario, "Soft robot

arm inspired by the octopus," *Adv. Robot.*, vol. 26, no. 7, pp. 709–727, 2012.

[52] T. George Thuruthel, E. Falotico, M. Manti, and C. Laschi, "Stable Open Loop Control of Soft Robotic Manipulators," *IEEE Robot. Autom. Lett.*, vol. 3, no. 2, pp. 1–1, 2018.

[53] M. C. Yip and D. B. Camarillo, "Model-Less Feedback Control of Continuum Manipulators in Constrained Environments," *IEEE Trans. Robot.*, vol. 30, no. 4, pp. 880–889, Aug. 2014.

[54] A. D'Souza, S. Vijayakumar, and S. Schaal, "Learning inverse kinematics," in *Intelligent Robots and Systems, 2001. Proceedings. 2001 IEEE/RSJ International Conference on*, 2001, vol. 1, pp. 298–303.

[55] T. George Thuruthel, Y. Ansari, E. Falotico, and C. Laschi, "Control Strategies for Soft Robotic Manipulators: A Survey," *Soft Robot.*, vol. 5, no. 2, p. soro.2017.0007, Apr. 2018.

[56] V. Pong, S. Gu, M. Dalal, and S. Levine, "Temporal difference models: Model-free deep rl for model-based control," *arXiv Prepr. arXiv1802.09081*, 2018.

[57] X. You *et al.*, "Model-free control for soft manipulators based on reinforcement learning," in *Intelligent Robots and Systems (IROS), 2017 IEEE/RSJ International Conference on*, 2017, pp. 2909–2915.

[58] H. Zhang, R. Cao, S. Zilberstein, F. Wu, and X. Chen, "Toward effective soft robot control via reinforcement learning," in *International Conference on Intelligent Robotics and Applications*, 2017, pp. 173–184.

[59] Y. Ansari, M. Manti, E. Falotico, M. Cianchetti, and C. Laschi, "Multiobjective optimization for stiffness and position control in a soft robot arm module," *IEEE Robot. Autom. Lett.*, vol. 3, no. 1, pp. 108–115, 2018.

[60] T. P. Lillicrap *et al.*, "Continuous control with deep reinforcement learning," 2015.

[61] V. K. Venkiteswaran and H.-J. Su, “A Three-Spring Pseudorigid-Body Model for Soft Joints With Significant Elongation Effects,” *J. Mech. Robot.*, vol. 8, no. 6, p. 61001, 2016.

[62] G. Singh and G. Krishnan, “A constrained maximization formulation to analyze deformation of fiber reinforced elastomeric actuators,” *Smart Mater. Struct.*, vol. 26, no. 6, p. 65024, Jun. 2017.

[63] E. G. Hocking and N. M. Wereley, “Analysis of nonlinear elastic behavior in miniature pneumatic artificial muscles,” *Smart Mater. Struct.*, vol. 22, no. 1, p. 14016, 2013.

[64] G. Krishnan, “Kinematics of a new class of smart actuators for soft robots based on generalized pneumatic artificial muscles,” in *IEEE International Conference on Intelligent Robots and Systems*, 2014, pp. 587–592.

[65] G. Krishnan, J. Bishop-Moser, C. Kim, and S. Kota, “Kinematics of a Generalized Class of Pneumatic Artificial Muscles,” *J. Mech. Robot.*, vol. 7, no. 4, p. 41014, Nov. 2015.

[66] C. S. Kothera, M. Jangid, J. Sirohi, and N. M. Wereley, “Experimental characterization and static modeling of McKibben actuators,” *J. Mech. Des.*, vol. 131, p. 91010, 2009.

[67] E. Azizi, E. L. Brainerd, and T. J. Roberts, “Variable gearing in pennate muscles,” *Proc. Natl. Acad. Sci.*, vol. 105, no. 5, pp. 1745–1750, 2008.

[68] R. Katz and Z. Li, “Kinematic and dynamic synthesis of a parallel kinematic high speed drilling machine,” *Int. J. Mach. Tools Manuf.*, vol. 44, no. 12–13, pp. 1381–1389, 2004.

[69] X. Zhang and G. Krishnan, “A nested pneumatic muscle arrangement for amplified stroke and force behavior,” *J. Intell. Mater. Syst. Struct.*, p. 1045389X1773092, Sep. 2017.

[70] B. Mosadegh *et al.*, “Pneumatic networks for soft robotics that actuate rapidly,” *Adv. Funct. Mater.*, vol. 24, no. 15, pp. 2163–2170, 2014.

[71] G. K. Klute and B. Hannaford, “Fatigue characteristics of McKibben artificial muscle

actuators," in *Intelligent Robots and Systems, 1998. Proceedings., 1998 IEEE/RSJ International Conference on*, 1998, vol. 3, pp. 1776–1781 vol.3.

[72] G. Krishnan, C. Kim, and S. Kota, "A Kinetostatic Formulation for Load-Flow Visualization in Compliant Mechanisms," *J. Mech. Robot.*, vol. 5, no. 2, p. 21007, 2013.

[73] S. K. Patiballa and G. Krishnan, "Qualitative Analysis and Conceptual Design of Planar Metamaterials With Negative Poisson's Ratio," *J. Mech. Robot.*, vol. 10, no. 2, p. 21006, Feb. 2018.

[74] S. Patiballa and G. Krishnan, "Qualitative Analysis and Design of Mechanical Metamaterials," in *Volume 5A: 41st Mechanisms and Robotics Conference*, 2017, p. V05AT08A002.

[75] K. Deb, A. Pratap, S. Agarwal, and T. Meyarivan, "A fast and elitist multiobjective genetic algorithm: NSGA-II," *IEEE Trans. Evol. Comput.*, vol. 6, no. 2, pp. 182–197, 2002.

[76] S. Patiballa, J. F. Shanley, and G. Krishnan, "Estimating Stress Bounds in Early-Stage Design of Distributed Compliant Mechanisms," in *Volume 5A: 40th Mechanisms and Robotics Conference*, 2016, p. V05AT07A017.

[77] N. Hansen, "The CMA evolution strategy: a comparing review," in *Towards a new evolutionary computation*, Springer, 2006, pp. 75–102.

[78] V. Mnih *et al.*, "Human-level control through deep reinforcement learning," *Nature*, vol. 518, no. 7540, p. 529, 2015.

[79] N. K. Uppalapati and G. Krishnan, "Design of Soft Continuum Manipulators Using Parallel Asymmetric Combination of Fiber Reinforced Elastomers." engrXiv, Aug-2018.

[80] N. K. Uppalapati, G. Singh, and G. Krishnan, "Parameter Estimation and Modeling of a

Pneumatic Continuum Manipulator with Asymmetric Building Blocks *," in *2018 IEEE International Conference on Soft Robotics (RoboSoft)*, 2018, pp. 2–7.

[81] V. Mnih *et al.*, "Playing atari with deep reinforcement learning," *arXiv Prepr. arXiv1312.5602*, 2013.

[82] J. Pan, Z. Chen, and P. Abbeel, "Predicting initialization effectiveness for trajectory optimization," in *2014 IEEE International Conference on Robotics and Automation (ICRA)*, 2014, pp. 5183–5190.

[83] G. Singh and G. Krishnan, "A constrained maximization formulation to analyze deformation of fiber reinforced elastomeric actuators," *Smart Mater. Struct.*, vol. 26, no. 6, p. 065024, Jun. 2017.